Journal of Electron Spectroscopy and Related Phenomena 200 (2015) 143–159

Contents lists available at ScienceDirect

Journal of Electron Spectroscopy and Related Phenomena

journal homepage: www.elsevier.com/locate/elspec

Zen and the art of dichroic photoemission

Gerrit van der Laan

Magnetic Spectroscopy Group, Diamond Light Source, Didcot OX11 0DE, United Kingdom

ARTICLE INFO

Article history:
Available online 14 June 2015

Keywords:
Angular dependent photoemission
Spin resolved
Linear and circular dichroism
Fundamental spectra
Chiral geometry
Sum rules

ABSTRACT

The discovery of magnetic dichroism in photoemission is celebrating its 25th anniversary this year. Here a review of the underlying general theory for the angular and spin dependence of dichroic core-level photoemission is presented using both a single-particle model and a many-body approach. The established methods of angular momentum coupling offer an elegant and powerful way to analyse the magnetic dichroism and spin polarization in photoemission from core and localized valence levels. In the presence of core-valence interactions one can distinguish different fundamental spectra, which via sum rules are related to physical properties described by coupled tensor operators for spin and orbital moments. By separating the angular dependence from the physical information, different geometries can be distinguished to measure the magnetic circular dichroism (MCD), linear dichroism (LD), circular dichroism in the angular dependence (CDAD), and magnetic linear dichroism in the angular dependence (MLDAD). Various ways to probe the core-hole polarization are discussed, such as using the angular dependence, moment analysis of the spectral distribution, and resonant photoemission decay.

1. Introduction

First observed in 1887 by Hertz [1], the photoelectric effect was explained in 1905 by Einstein [2] as caused by the emission of electrons when a material is irradiated with light. Photoemission measurements on solids gained popularly in the 1970s with the appearance of ultra-high vacuum conditions, able to maintain clean surfaces, and high-resolution electron energy analysers, single-electron counting technique and image plates. A further spur came from the advent of synchrotron radiation sources in the 1980s. A wide array of techniques has since become available, such as angle- and spin-resolved photoemission, isochromat spectroscopy and resonant photoemission.

For long it was commonly believed that core level photoemission would not depend on the linear or circular polarization of the incident photons, except near threshold. It came therefore as a large surprise in 1990 when Baumgarten et al. [3] reported the magnetic circular dichroism (MCD) in core-level photoemission from ferromagnets, which was soon confirmed by others [4,5]. It was found that the dichroism did not disappear when the magnetization direction is perpendicular to the light helicity vector [6]. A strong dichroism was observed at the surface of Ni metal due to an enhanced orbital moment [7], and MCD was also reported in resonant photoemission [8].

Reversing the magnetization direction perpendicular to the plane of measurement in a chiral geometry gave rise to a new effect called magnetic linear dichroism in the angular dependence (MLDAD) in photoemission, as first reported in 1993. [9–11] A year later, it was explained as being due to the interference between the two outgoing photoemission channels [12,13].

An invaluable method to the analysis of the photoelectron distribution in a complete experiment, as determined by the photon energy, kinetic energy, emission angle, magnetization direction, crystal orientation and spin direction, is the separation of the transition probability into a dynamic (or physical) part and a geometric (or angular) part. Photoemission is rarely measured angle integrated, instead only a narrow cone of emitted electrons is collected by the analyser. In crystalline and magnetic samples the experiment is then characterized by at least three vectors, i.e., those of the crystal orientation or magnetization direction, **M**, the light polarization, **P**, and the electron emission direction, ε. Additionally, spin resolved photoemission has the spin direction, $\mathbf{P}_S$, of the emitted electron. When these vectors are coplanar the analysis is fairly straightforward, although the emission intensity and spin polarization will strongly depend on the angles. When these vectors are collinear the photoemission is even simpler to analyse and resembles in some aspects the simple case of angle integrated emission, where interesting effects remain hidden. However, when the three vectors are neither coplanar nor mutually perpendicular, the geometry can have a handedness. This means that if one of the odd vectors is reversed, such as the magnetization or the light helicity,

E-mail address: gerrit.vanderlaan@diamond.ac.uk

http://dx.doi.org/10.1016/j.elspec.2015.06.001

the opposite handedness is obtained, which gives a change in the photoemission signal. Such geometries turn out to be of great interest. Whilst a combination of isotropic and linear polarized light can be obtained by adding up the contributions from left and right circularly polarized light, the opposite, creating circularly polarized light from linearly polarized light is excluded by parity conservation. However, by using the handedness (chirality) of the photoemission geometry, it becomes possible to measure with linear polarization the same dichroic spectrum as with circular polarization.

Core-level photoemission has become an important tool for the study of the electronic and magnetic properties of transition metal, rare earth and actinide compounds [14–18]. The presence of core-valence interactions in the final state is evidenced by the occurrence of multiplet structure and charge-transfer satellites in spectra, which allows to extract details about the character of the ground state [19]. The advent of sophisticated insertion devices for polarized synchrotron radiation have enabled the exploration of the polarization dependence in the core excitations.

This paper presents a theoretical overview and treats dichroic photoemission in a wider context, evoking fundamental spectra, moment analysis, core-hole polarization, and resonant decay processes. These topics are captured by the elegant methods of angular momentum coupling, which provide very general solutions, not only for atomic spectroscopy but also for other disciplines such as, e.g., nuclear shell theory [20]. We will present the more general and practical aspects of dichroic photoemission with the emphasis on fundamental spectra, angular dependence and chirality. By recoupling the expression for the transition probability we can separate the geometric and dynamic part. The latter describes the physical properties of the atom, containing information about the properties connected with the electron shell, as well as the relationship between these states and the final state.

We will proceed by following a series of papers by Thole and van der Laan, [21,22,12,23], which give a rather complete account of the theory for spin polarization and circular and linear dichroism in photoemission from core and valence states in localized magnetic systems. After a description of the basic principles in Section 2, [24] first the angle-integrated photoemission is analyzed in Section 3. [21] This provides a solid basis to introduce the fundamental spectra, which in the presence of electrostatic interactions give the correlation between the spin and orbital moments of the core and valence electrons. We discuss the emission from both one-electron states [25] and multi-electronic configurations. Sum rules relate the integrated intensities of the spectra to the expectation values of ground state operators, given by coupled tensor operators [22]. The spectral distribution allows us to extract information about higher order moments [26]. The angular dependence is treated in Section 4. The geometry can be separated from the physical part, which gives the fundamental spectra. The angular distribution exposes the higher multipole moments. Section 5 discusses in more detail the geometrical aspects, where a chiral geometry leads to MLDAD and CDAD. Using group theory it is shown that these spectra form independent linear combinations. Section 6 briefly shows how crystal field symmetry can be implemented into the theory. Section 7 gives a concise comparison with X-ray absorption spectroscopy (XAS) and also discusses the core-hole polarization. Section 8 presents the theory of spin polarization and magnetic dichroism in resonant photoemission decay. Compared to XAS, it can measure different linear combinations of ground state moments. Finally, several illustrations are presented in Section 9. The correlation between spin and orbital moments is extracted from the fundamental spectra in the case of the Gd 4*d* photoemission. The influence of the diffraction effects is shown. The MCD and MLDAD are shown to be equivalent in the case of hard X-ray photoemission. Conclusions are drawn in Section 10.

2. Basic principles

Some insight in the philosophy on which the dichroic photoemission rests can be obtained by considering a core level ℓ which is split into orbital sublevels m. When these sublevels are energy degenerated, the core state has a spherical symmetry. By lifting the degeneracy, the sublevels will split in energy and have distinctly different orbital moments. The core-hole sublevel splitting is caused by the electrostatic interaction with the magnetically polarized valence electrons. Alternatively, in a one-electron model, the splitting can be described as due to an effective spin field in combination with spin–orbit interaction to split the orbital sublevels. For each sublevel m, the dipole transition probability is different for left- ($\Delta m = -1$) and right- ($\Delta m = +1$) circularly polarized radiation. For instance, for emission from a sublevel $m = \ell$ to the continuum state $c = \ell - 1$ with components γ, where $-\ell + 1 \le \gamma \le \ell - 1$, the transition $\Delta m = -1$ is allowed, but the transition $\Delta m = +1$ is not possible. Thus the polarized core state gives rise to a strong circular dichroism in photoemission.

An important ingredient is the conservation of angular momentum in the transition. This is easy to see in angle integrated photoemission, where the emitted electron distribution has zero moment, so that the light transfers its full moment to the atom. We can make new linear combinations of the polarized spectra, the so called fundamental spectra I^{xy}, in which the electric-dipole radiation transfers an orbital moment of $x = 0$, 1, or 2 for the isotropic spectrum, circular, and linear dichroism, respectively, and the photoelectron spin carries away a moment $y = 0$ or 1 in the case without and with spin detection, respectively. Then, the spectra I^{xy} give the probability for removing an electron with moments x and y. In the presence of core-valence interactions, these fundamental spectra will reveal the correlation between spin and orbital moments of the core hole and the valence band. Moreover, the integrated intensities of the fundamental spectra give the expectation values of the spin and orbital moments of the emitting shell. For instance, the magnetic circular dichroism and spin spectrum relate to the ground state orbital and spin magnetic moment, respectively. This is particularly useful in the case of the localized 4*f* shell of the rare earths, which is partly filled.

Since lifting the energy degeneracy leads to an anisotropic charge distribution, the core hole polarization can be measured in angle dependent photoemission. Using momentum conservation we can tackle the angular dependent photoemission, by considering that the emitted photoelectron carries away a moment, which is even due to parity ($b = 0$, 2, or 4). Now, each fundamental spectrum produces a limited set of angular distributions. Higher moments of the atom can be reached compared to angle-integrated photoemission. Interference effects between the two different continuum states gives rise to 'odd' waves, which can be observed in a chiral geometry, spanned by the three vectors of the light polarization, magnetization and emission direction.

We will describe resonant photoemission as a two-step process in which the first step is X-ray absorption that gives a polarized core hole and an additional valence electron. In the second step the core hole decays by Coulomb interaction under emission of an electron whereby a two-hole state is created. In XAS (and XMCD) the sum rules measure only the number of holes (monopole moment) in the core level, and the core hole polarization manifests itself in the spectral line shape. The angular dependence of the resonant photoemission allows us to obtain also the higher moments of the core hole. Compared to XAS, this gives new sum rules which measure different combinations of the ground state moments.

In the following, we use the theory of second quantization to write the transition probability in terms of creation and annihilation operators. This enables us to derive formulae that do not dependent on the precise nature of the initial and final states, and

are thus independent of the coupling scheme. In this way a maximum amount of information can be acquired using a minimum number of constraints. The quantum theory of angular momentum will be used to recouple the transition matrix elements.

3. Angle-integrated photoemission

Consider an initial state $|\psi\rangle$ containing electrons in atomic shell ℓ with orbital and spin components m and σ, respectively. The state $|\psi\rangle$ may contain also other closed shells and open shells interacting with the shell ℓ by electrostatic interactions. Electric 2^Q-pole transitions with light polarization q are allowed for $|c-Q| \le \ell \le c+Q$ (with $c+Q+\ell$ even) to final states $|\psi', c\gamma\sigma\rangle$, containing an electron in a continuum state c with orbital and spin components γ and σ, respectively. We assume that c has no interactions with the rest of the system. The light acts only on the orbital part, which means the spin component σ is conserved in the transition. The transition matrix element for $\ell \to c$ photoemission is given as

$$\begin{aligned} T^Q_{q\sigma} &= \sum_{m\gamma} \langle \psi', c\gamma\sigma | c^\dagger_{\gamma\sigma} \ell_{m\sigma} | \psi\rangle \langle \ell m | C^Q_q | c\gamma\rangle \\ &= \sum_{m\gamma} \langle \psi' | \ell_{m\sigma} | \psi\rangle \langle \ell m | C^Q_q | c\gamma\rangle, \end{aligned} \tag{1}$$

where $\ell_{m\sigma}$ is the annihilation operator of an electron in shell ℓ and $c^\dagger_{\gamma\sigma}$ is the creation operator of an electron in continuum state c, and $C^Q_q(\theta,\phi)$ is the normalized spherical harmonic for the light polarization q (with $q = -Q, -Q+1, \ldots, Q$). Restricting us in this section to angle-integrated photoemission means we can sum over γ. The photoemission intensity is equal to

$$\begin{aligned} I^Q_{q'\sigma'q\sigma} &= \sum_{m'm\gamma} T^{Q*}_{q'\sigma'} T^Q_{q\sigma} = \sum_{m'm\gamma} \langle \psi | \ell^\dagger_{m'\sigma'} | \psi'\rangle \langle \psi' | \ell_{m\sigma} | \psi\rangle \, |\langle \ell \| T^Q \| c\rangle|^2 \\ &\times (-)^{2\ell-m'-m} \begin{pmatrix} \ell & Q & c \\ -m' & q' & \gamma \end{pmatrix} \begin{pmatrix} \ell & Q & c \\ -m & q & \gamma \end{pmatrix}, \end{aligned} \tag{2}$$

with a reduced matrix element

$$\langle \ell \| T^Q \| c\rangle \equiv [\ell c] \begin{pmatrix} \ell & Q & c \\ 0 & 0 & 0 \end{pmatrix} R^{\ell Qc}, \tag{3}$$

where we introduced the shorthand notation $[\ell\, c] = (2\ell+1)(2c+1)$. The radial matrix element $R^{\ell Qc}$ is a function of the kinetic energy but varies only slowly over the narrow range of the core level spectrum [27].

The 3j-symbol (or Wigner coefficient)—denoted by the parentheses—is related to the well-known Clebsch-Gordan coefficient $\langle \ell\, mQq | c\gamma\rangle$,

$$\begin{pmatrix} \ell & Q & c \\ -m & q & \gamma \end{pmatrix} = (-)^{\ell-m} [\ell]^{-1/2} \langle \ell m Q q | c\gamma\rangle, \tag{4}$$

but the use of 3j-symbols is favoured because they have higher symmetry properties [28,29]. Their value can be obtained, e.g., by using freely available calculators on the Internet. The 3j-symbol is zero unless the following conditions are satisfied: $\ell+Q+c$, which is an integer, is even if $m = q = \gamma = 0$ (parity rule), $c+Q \ge \ell$ and $\ell+Q \ge c$ and $\ell+c \ge Q$ (triangle inequalities), and $-m+q+\gamma = 0$ (rotational invariance). We immediately recognize these as the relevant physical conditions for angular momentum conservation, i.e., the selection rules for optical transitions.

The spectra $I_{q'\sigma'q\sigma}$ depend on the final core-hole state $|\psi'\rangle$ and by using energy conservation they can be written as a function of the photon energy ω, photoelectron kinetic energy E_k, and initial- and final-state energies E_g and E_f,

$$I^Q_{q'\sigma'q\sigma}(E,\omega) = \sum_f I^Q_{q'\sigma'q\sigma}(f)\, \delta(E + E_f - \omega - E_g). \tag{5}$$

The energy δ-function plays no role in the momentum coupling and hence shall be omitted in the following.

3.1. Definition of the fundamental spectra

Fundamental spectra $I^{xy}_{\xi\eta}$ are defined as linear combinations of the primitive spectra $I_{q'\sigma'q\sigma}$, where we introduce the multipole moments x and y with components ξ and η, respectively,

$$\begin{aligned} I^{xy}_{\xi\eta} &\equiv n^{-1}_{Qx} n^{-1}_{sy} \sum_{qq'\sigma\sigma'} (-)^{Q-q'+s-\sigma'} \\ &\times \begin{pmatrix} Q & x & Q \\ -q' & \xi & q \end{pmatrix} \begin{pmatrix} s & y & s \\ -\sigma' & \eta & \sigma \end{pmatrix} I_{q'\sigma'q\sigma} \end{aligned} \tag{6}$$

with $s = 1/2$ and normalization factors

$$n_{Qx} \equiv \begin{pmatrix} Q & x & Q \\ -Q & 0 & Q \end{pmatrix} = \frac{(2Q)!}{\sqrt{(2Q-x)!(2Q+1+x)!}}, \tag{7}$$

which remove the square roots. In I^{xy} we omit the index Q to reduce cluttering. The light polarization and photoemission spin have moments a and h, respectively. Due to momentum conservation, in angular integrated photoemission they correspond to the orbital moments x (= a) and spin moment y (= h) of the shell ℓ, as we will derive in Section 3.2. Eq. (6) can be written as

$$I^{xy}_{\xi\eta} = \sum_{qq'\sigma\sigma'} V^{Qx}_{q'q\xi} V^{sy}_{\sigma'\sigma\eta} I_{q'\sigma'q\sigma}, \tag{8}$$

by using the notation for the normalized 3j-symbols

$$V^{Qx}_{q'q\xi} \equiv n^{-1}_{Qx} (-)^{Q-q'} \begin{pmatrix} Q & x & Q \\ -q' & \xi & q \end{pmatrix}, \tag{9}$$

$$V^{sy}_{\sigma'\sigma\eta} \equiv n^{-1}_{sy} (-)^{s-\sigma'} \begin{pmatrix} s & y & s \\ -\sigma' & \eta & \sigma \end{pmatrix}. \tag{10}$$

The triad (QxQ) gives the triangle condition $x = 0, 1, \ldots, 2Q$ with components $\xi = q' - q$, where $-x \le \xi \le x$. Eq. (9) can be written out as a two-dimensional matrix of rank [Q] with elements $q'q$,

$$V^{Qx}_{\xi} = \sum_{q'q} |Qq'\rangle V^{Qx}_{q'q\xi} \langle Qq| \equiv \sum_{q'q} Q^*_{q'} Q_q V^{Qx}_{q'q\xi}, \tag{11}$$

where $Q^*_q = (-)^q Q_{-q}$. For instance, for $Q = 1$ (denoted here as L),

$$V^{L0}_{\xi} = \begin{pmatrix} 1 & 0 & 0 \\ 0 & 1 & 0 \\ 0 & 0 & 1 \end{pmatrix}, V^{L1}_{\xi} = \begin{pmatrix} 1 & -1 & 0 \\ 1 & 0 & -1 \\ 0 & 1 & -1 \end{pmatrix},$$

$$V^{L2}_{\xi} = \begin{pmatrix} 1 & -\sqrt{3} & \sqrt{6} \\ \sqrt{3} & -2 & \sqrt{3} \\ \sqrt{6} & -\sqrt{3} & 1 \end{pmatrix}.$$

By convention, the first, second and third element in the top row correspond to $|1\rangle\langle 1|$, $|1\rangle\langle 0|$, and $|1\rangle\langle -1|$ (i.e., $L^*_1 L_1$, $L^*_0 L_1$, and $L^*_{-1} L_1$), respectively.

The V^{Lx}_{ξ} can be separated in its different ξ ($=m'-m$) values, by taking the coefficients on a line parallel to the diagonal of the matrix, which gives a scalar, vector, and tensor, respectively,

$$V^{10}_0 = \frac{1}{2}(L^*_1L_1 + L^*_0L_0 + L^*_{-1}L_{-1}), \tag{12}$$

$$\begin{aligned} V^{11}_1 &= L^*_0L_1 + L^*_{-1}L_0, \\ V^{11}_0 &= -L^*_1L_1 + L^*_{-1}L_{-1}, \\ V^{11}_{-1} &= -L^*_1L_0 - L^*_0L_{-1}, \end{aligned} \tag{13}$$

$$\begin{aligned} V^{12}_2 &= -\sqrt{6}\, L^*_{-1}L_1, \\ V^{12}_1 &= -\sqrt{3}(-L^*_0L_1 + L^*_{-1}L_0), \\ V^{12}_0 &= -(L^*_1L_1 - 2L^*_0L_0 + L^*_{-1}L_{-1}), \\ V^{12}_{-1} &= -\sqrt{3}(L^*_1L_0 - L^*_0L_{-1}), \\ V^{12}_{-2} &= -\sqrt{6}\, L^*_1L_{-1}, \end{aligned} \tag{14}$$

This result can be verified by substituting the familiar orbital momentum matrices

$$L_1 = \begin{pmatrix} 0 & -1 & 0 \\ 0 & 0 & -1 \\ 0 & 0 & 0 \end{pmatrix}, L_0 = \begin{pmatrix} 1 & 0 & 0 \\ 0 & 0 & 0 \\ 0 & 0 & -1 \end{pmatrix},$$

$$L_{-1} = \begin{pmatrix} 0 & 0 & 0 \\ 1 & 0 & 0 \\ 0 & 1 & 0 \end{pmatrix},$$

into Eqs. (12)-(14), which returns the matrices V^{Lx}_{ξ} [30].

For the spin, the triad (*sys*) in Eq. (10) gives the triangle condition $y = 0, 1$ with components $\eta = \sigma' - \sigma$, where $-y \le \eta \le y$. It can be written as a two-dimensional matrix V^{sy}_{η} of rank 2 with elements $\sigma'\sigma$,

$$V^{s0}_{\eta} = \begin{pmatrix} 1 & 0 \\ 0 & 1 \end{pmatrix}; \quad V^{s1}_{\eta} = \begin{pmatrix} 1 & -\sqrt{2} \\ \sqrt{2} & -1 \end{pmatrix}.$$

Such matrices are useful to evaluate the spectra in a crystal field with arbitrary point-group symmetry, as briefly discussed in Section 6.

In cylindrical symmetry (SO_2) with field along the z-axis, there are no cross terms (i.e., $m' = m$), so that $\xi = 0$, and taking the spin direction along the same axis, $\sigma' = \sigma$, so that $\eta = 0$, only the spectra I^{xy}_{00} exist, giving $(2\ell+1)(2s+1)$ spectra called I^{xy}. Then we require only the diagonal elements, $V^{Qx}_q \equiv V^{Qx}_{q'q\xi}\delta_{\xi,0}$, which have the simple analytical form

$$V^{Q0}_q = 1, \tag{15a}$$

$$V^{Q1}_q = \frac{q}{Q}, \tag{15b}$$

$$V^{Q2}_q = \frac{3q^2 - Q(Q+1)}{Q(2Q-1)}, \tag{15c}$$

$$V^{Q3}_q = \frac{5q^3 - q(3Q^2-1)}{Q(Q-1)(2Q-1)}, \tag{15d}$$

etc. For dipole transitions ($Q = 1$), Eq. (8) gives for the x moment $I^0 = I_1 + I_0 + I_{-1}$, $I^1 = I_1 - I_{-1}$, and $I^2 = I_1 - 2I_0 + I_{-1}$, which correspond to the isotropic spectrum and the circular and linear dichroism, respectively.

Similarly, for the y-moment we obtain $I^0 = I_\uparrow + I_\downarrow$ and $I^1 = I_\uparrow - I_\downarrow$, where $\sigma = \frac{1}{2}, -\frac{1}{2}$ is denoted by $\uparrow, \downarrow$, respectively. Thus $y = 0$ and 1 correspond to the measurement without and with spin detection, respectively. Combined, this gives the fundamental spectra I^{xy} as the linear combination of $I_{q\sigma}$ listed in Table 1. In the presence of spin–orbit interaction, x and y couple to a moment z of the total angular momentum j, which gives the fundamental spectra

$$I^{xyz}_{\zeta} \equiv n^{-1}_{xyz}\sum_{\xi\eta} I^{xy}_{\xi\eta} \begin{pmatrix} x & z & y \\ \xi & \zeta & \eta \end{pmatrix}, \tag{16}$$

with $|x-y| \le z \le x+y$ and $x+y+z$ = even. The normalization constant is defined as [12,31]

$$n_{abc} \equiv \begin{pmatrix} a & b & c \\ 0 & 0 & 0 \end{pmatrix}, \tag{17}$$

for $a+b+c$ = even. Note that

$$I^{xy} = \sum_z I^{xyz}. \tag{18}$$

Our situation would be ideal if we could measure

$$I^{xyz} \propto \sum_{q\sigma M} I_{q\sigma M} V^{Qx}_q V^{sy}_{\sigma} V^{Jz}_M, \tag{19}$$

in which case all eight spectra I^{xyz} could be separated, but this clearly requires $I_{q\sigma M}$ to be measured for all M, which is impractical because we would have to populate those M sublevels specifically. Therefore, in practise we work with I^{xy} with the minor disadvantage that for two spectra z is summed over two terms [21]. We shall return to this in Section 3.3, when we discuss the fundamental spectra of one-electron states.

3.2. Physical meaning of fundamental spectra

Now we know how to make the fundamental spectra (Table 1), we also need to understand their meaning. The spectra I^{xy} give the probability for removing an electron with moments x and y. The I^{00} spectrum is independent of the external field. The other spectra require an external field, i.e., exchange and/or Coulomb interaction to correlate the moment of the core electron with that of the valence electrons. An odd value of x involves an oriented orbital moment (dipole, octupole, etc) and an even value of x involves a (magnetically or electrostatically) aligned orbital moment (quadrupole or hexadecapole, etc).

To recouple Eq. (2), we use the relation YLV4 [32–34],

$$\begin{aligned} &\sum_{\gamma}(-)^{c-\gamma} \begin{pmatrix} \ell & Q & c \\ -m & q & \gamma \end{pmatrix} \begin{pmatrix} \ell' & Q' & c \\ -m' & q' & \gamma \end{pmatrix} \\ &= \sum_{x\xi}(-)^{\ell'+Q+c-\xi}[x] \begin{Bmatrix} \ell & x & \ell' \\ Q' & c & Q \end{Bmatrix} \\ &\times \begin{pmatrix} Q' & x & Q \\ -q' & \xi & q \end{pmatrix} \begin{pmatrix} \ell' & x & \ell \\ -m' & \xi & m \end{pmatrix}, \end{aligned} \tag{20}$$

where the product of two 3j-symbols is summed over γ. The result is then substituted into Eq. (6) (omitting the radial matrix element given in Eq. (3)), and the orthogonality relations of the 3j-symbols

Table 1
Angle-integrated photoemission: Fundamental spectra I^{xy} for $Q = 1$ as linear combinations of primitive spectra $I_{q\sigma}$, where $\sigma = \frac{1}{2}, -\frac{1}{2}$ is denoted by ↑, ↓, respectively. The last column gives the sum rules for the integrated intensities ρ^{xy}, which can be related to the spin and orbital moments of the ℓ shell.

Photoemission spectrum	$I^{xy} = \sum_{q\sigma} I_{q\sigma}$	$\rho^{xy} = \int I^{xy} dE$
Isotropic spectrum	$I^{00} = I_{1\uparrow} + I_{0\uparrow} + I_{-1\uparrow} + I_{1\downarrow} + I_{0\downarrow} + I_{-1\downarrow}$	$\rho^{00} \propto \langle n \rangle$
Spin spectrum	$I^{01} = I_{1\uparrow} + I_{0\uparrow} + I_{-1\uparrow} - I_{1\downarrow} - I_{0\downarrow} - I_{-1\downarrow}$	$\rho^{01} \propto \langle S_z \rangle$
Orbit spectrum (MCD)	$I^{10} = I_{1\uparrow} - I_{-1\uparrow} + I_{1\downarrow} - I_{-1\downarrow}$	$\rho^{10} \propto \langle L_z \rangle$
Spin–orbit spectrum	$I^{11} = I_{1\uparrow} - I_{-1\uparrow} - I_{1\downarrow} + I_{-1\downarrow}$	$\rho^{11} \propto \langle \sum_i \ell_z(i) s_z(i) \rangle$
Anisotropic spectrum (MLD)	$I^{20} = I_{1\uparrow} - 2I_{0\uparrow} + I_{-1\uparrow} + I_{1\downarrow} - 2I_{0\downarrow} + I_{-1\downarrow}$	$\rho^{20} \propto \langle Q_z \rangle$
Anisotropic spin spectrum	$I^{21} = I_{1\uparrow} - 2I_{0\uparrow} + I_{-1\uparrow} - I_{1\downarrow} + 2I_{0\downarrow} - I_{-1\downarrow}$	$\rho^{21} \propto \langle \sum_i q_z(i) s_z(i) \rangle$

(QxQ) is used. Similarly, the spin is recoupled, finally obtaining

$$I^{xy}_{\xi\eta}(\psi') = A^{Qc\ell}_x n^{-1}_{\ell x} n^{-1}_{sy} [xy] \sum_{m'\sigma' m\sigma} \langle\psi|\ell^\dagger_{m'\sigma'}|\psi'\rangle\langle\psi'|\ell_{m\sigma}|\psi\rangle \times (-)^{\ell-m+s-\sigma} \begin{pmatrix} \ell & x & \ell \\ -m' & \xi & m \end{pmatrix} \begin{pmatrix} s & y & s \\ -\sigma' & \eta & \sigma \end{pmatrix},$$

$$= A^{Qc\ell}_x [xy] \sum_{m'\sigma' m\sigma} \langle\psi|\ell^\dagger_{m'\sigma'}|\psi'\rangle\langle\psi'|\ell_{m\sigma}|\psi\rangle V^x_{\ell m' m} V^y_{s\sigma'\sigma}. \quad (21)$$

The 3j-symbols give the orbit moment with $x = 0, \ldots, 2\ell$ and spin moment $y = 0, 1$. The coefficient

$$A^{Qc\ell}_x \equiv (-)^{\ell+c+Q+x} \begin{Bmatrix} \ell & x & \ell \\ Q & c & Q \end{Bmatrix} n_{\ell x} n^{-1}_{Qx}, \quad (22)$$

contains a 6j-symbol, which gives the coupling coefficient of moment x in the product of Q and ℓ when they combine to c. Evaluating some elements gives [34]

$$A^{Qc\ell}_0 = \frac{1}{[\ell]} \equiv A^\ell_0, \quad (23a)$$

$$A^{Qc\ell}_1 = \frac{Q(Q+1) + \ell(\ell+1) - c(c+1)}{2Q(\ell+1)[\ell]}. \quad (23b)$$

The stretched members ($c = \ell \pm Q$) are Q independent, namely

$$A^{Q,\ell-Q,\ell}_x = \frac{1}{[\ell]}, \quad (24a)$$

$$A^{Q,\ell+Q,\ell}_1 = -\frac{1}{[\ell](\ell+1)}, \quad (24b)$$

$$A^{Q,\ell+Q,\ell}_2 = \frac{\ell(2\ell-1)}{[\ell](\ell+1)(2\ell+3)}. \quad (24c)$$

The coefficients $A^{Qc\ell}_x$ give the intensities for the different emission channels c. Eq. (24b) shows that for I^{10} the intensities of the two emission channels $c = \ell \pm Q$ have opposite sign.

3.3. One-electron states

The fundamental spectra for one-electron states, i.e., using an independent electron model, are easy to derive. They are perhaps not a realistic representation of the reality, but serve the useful purpose of a demonstration.

Taking an initial core-state sublevel $|\phi\rangle = \sum_{m\sigma} |\ell\, m\sigma\rangle$ and a final state $|\phi', c\gamma\sigma\rangle$, where $|\phi'\rangle = |0\rangle$, the operator part for the one-electron state reduces as

$$\langle\phi|\ell^\dagger_{m\sigma}|0\rangle\langle 0|\ell_{m\sigma}|\phi\rangle = \langle\phi|\ell^\dagger_{m\sigma}\ell_{m\sigma}|\phi\rangle = \langle n_{m\sigma}\rangle, \quad (25)$$

where $n_{m\sigma}$ is the occupation number operator (cf. density matrix) of the core sublevel with components m, σ. Eq. (21) gives the intensities of the sublevels ϕ as [25]

$$I^{xy}(\phi) = A^{Qc\ell}_x \sum_{m\sigma} \langle n_{m\sigma}\rangle V^{\ell x}_m V^{sy}_\sigma. \quad (26)$$

Omitting the coefficient $A^{Qc\ell}_x$ and using Eq. (15) this gives for arbitrary one-electron wave function ϕ,

$$I^{00}(\phi) = \sum_{m\sigma} \langle n_{m\sigma}\rangle = \langle n\rangle, \quad (27a)$$

$$I^{01}(\phi) = \sum_{m\sigma} \langle n_{m\sigma}\rangle \frac{\sigma}{s} = \frac{\langle s_z\rangle}{s}, \quad (27b)$$

$$I^{10}(\phi) = \sum_{m\sigma} \langle n_{m\sigma}\rangle \frac{m}{\ell} = \frac{\langle \ell_z\rangle}{\ell}, \quad (27c)$$

$$I^{11}(\phi) = \sum_{m\sigma} \langle n_{m\sigma}\rangle \frac{m\sigma}{\ell s} = \frac{\langle \ell_z \cdot s_z\rangle}{\ell s}, \quad (27d)$$

$$I^{20}(\phi) = \sum_{m\sigma} \langle n_{m\sigma}\rangle \frac{3m^2 - \ell(\ell+1)}{\ell(2\ell-1)} = \frac{3\langle q_z\rangle}{\ell(2\ell-1)}, \quad (27e)$$

$$I^{21}(\phi) = \sum_{m\sigma} \langle n_{m\sigma}\rangle \frac{[3m^2 - \ell(\ell+1)]\sigma}{\ell(2\ell-1)s} = \frac{3\langle q_z \cdot s_z\rangle}{2\ell(2\ell-1)}, \quad (27f)$$

where n is the number of electrons, s_z the spin moment, ℓ_z the orbital moment and q_z the quadrupole moment of the ℓ shell.

A deep core level with $\ell \neq 0$ will be split by spin–orbit interaction ζ. To account for core-valence interactions, we assume an effective magnetic field H_s on the core shell, induced by the polarized valence states [35]. This field splits each core level $j = \ell \pm s$ into sublevels m_j. Assuming that $H_s \ll \zeta$, the energy of the sublevels is

$$E_{jm_j} = H_s m_j \frac{j(j+1) + s(s+1) - \ell(\ell+1)}{2j(j+1)}, \quad (28)$$

with wave functions $|jm_j\rangle$ as a sum over $|m, \sigma\rangle$ states

$$|jm_j\rangle = \sum_{m\sigma} (-)^{j-m_j} [j]^{1/2} \begin{pmatrix} j & \ell & s \\ -m_j & m & \sigma \end{pmatrix} |m\sigma\rangle. \quad (29)$$

As an example, consider the sublevels of the p shell (ℓ=1) shown in Table 2. For $\phi = |3/2, 3/2\rangle$, Eq. (3.3) gives that $I^{xy} = 1$ for all xy, while for $\phi = |3/2, 1/2\rangle$ we obtain $I^{00} = 1$, $I^{01} = I^{10} = 1/3$, $I^{11} = -1/3$, $I^{20} = -1$, $I^{21} = -5/3$. This alerts us to the fact that for a mixed $|m, \sigma\rangle$ state

$$\sum_{m\sigma} \langle n_{m\sigma}\rangle m\sigma \neq \sum_{m\sigma} \langle n_{m\sigma}\rangle m \cdot \sum_{m\sigma} \langle n_{m\sigma}\rangle \sigma. \quad (30)$$

Table 2
The states $|jm_j\rangle$ of a p core level given as linear combinations over states $|m\sigma\rangle$.

j	m_j	$\sum_{m\sigma} c_{m\sigma} \lvert m\sigma\rangle$
3/2	−3/2	$\lvert -1\downarrow\rangle$
	−1/2	$\sqrt{2/3}\lvert 0\downarrow\rangle + \sqrt{1/3}\lvert -1\uparrow\rangle$
	+1/2	$\sqrt{1/3}\lvert 1\downarrow\rangle + \sqrt{2/3}\lvert 0\uparrow\rangle$
	+3/2	$\lvert 1\uparrow\rangle$
1/2	+1/2	$\sqrt{2/3}\lvert 1\downarrow\rangle - \sqrt{1/3}\lvert 0\uparrow\rangle$
	−1/2	$\sqrt{1/3}\lvert 0\downarrow\rangle - \sqrt{2/3}\lvert -1\uparrow\rangle$

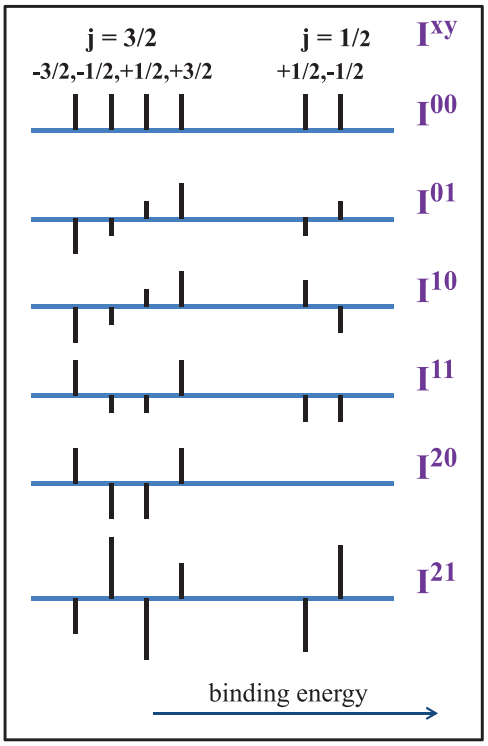

Fig. 1. Fundamental spectra $I^{xy}(jm_j)$ for p-shell photoemission in the jj coupling limit ($H_s \ll \zeta$) using the one-electron model.

Calculating the intensities for all sublevels of the p shell, the one-particle spectra $I^{xy}(jm_j)$ are plotted in Fig. 1. [36,37] From the patterns of the line intensities it is evident that the I^{xy} spectra can be expressed as a sum over $V^{jz}_{m_j}$ distributions, where $|x-y| \le z \le x+y$, with $x+y+z$ even and $z \le 2j$. Table 3 gives the spectra for $j = 3/2$ and 1/2 as $V^{jz}_{m_j}$ distributions that are given in Table 4. Note that $V^{jz}_{m_j}$ are orthogonal functions since $\sum_{m_j} V^{jz}_{m_j} V^{jz'}_{m_j} = [j]\delta_{zz'}$.

For I^{x0} the distribution over the jm_j sublevels is [37]

$$I^{x0}(jm_j) = [j\ell] A^{Qc\ell}_x A^{\ell sj}_x V^{jx}_{m_j}, \tag{31}$$

Table 3
Fundamental spectra I^{xyz} for p-shell photoemission in the one-electron model as moments $V^z \equiv V^{jz}_{m_j}$, which are given in Table 4. Note that $I^{xy} = \sum_z I^{xyz}$.

I^{xyz}	$j = \frac{3}{2}$	$j = \frac{1}{2}$
I^{000}	V^0	V^0
I^{011}	V^1	$-\frac{1}{3}V^1$
I^{101}	V^1	$\frac{2}{3}V^1$
I^{110}	$\frac{1}{3}V^0$	$-\frac{2}{3}V^0$
I^{112}	$-\frac{2}{3}V^2$	0
I^{202}	V^2	0
I^{211}	$\frac{2}{5}V^1$	$-\frac{4}{3}V^1$
I^{213}	$\frac{3}{5}V^3$	0

Table 4
Coefficients $V^z \equiv V^{jz}_{m_j}$ for the m_j sublevels of $j = 3/2$ and 1/2.

	$j = \frac{3}{2}$				$j = \frac{1}{2}$	
m_j	$-\frac{3}{2}$	$-\frac{1}{2}$	$\frac{1}{2}$	$\frac{3}{2}$	$\frac{1}{2}$	$-\frac{1}{2}$
V^0	1	1	1	1	1	1
V^1	−1	$-\frac{1}{3}$	$\frac{1}{3}$	1	1	−1
V^2	1	−1	−1	1	0	0
V^3	−1	3	−3	1	0	0

which gives

$$j = \ell + s: \quad I^{x0}(jm_j) = V^{jx}_{m_j},$$
$$j = \ell - s: \quad I^{x0}(jm_j) = V^{jx}_{m_j} \frac{(2\ell - x)(2\ell + x + 1)}{2\ell[\ell]}.$$

Thus the set of I^{x0} spectra is clearly orthogonal, but this exhausts the number of orthogonal spectra possible ($x \le 2j$). Spectra with equal z have the same distribution. Table 3 shows a one-to-one relation between fundamental spectra and spectral distributions: $I^{xyz}(jm_j) \propto V^{jz}_{jm_j}$, where $I^{xy} = \sum_z I^{xyz}$.

The expectation value of the spin–orbit interaction is

$$\langle \ell s j | \ell \cdot s | \ell s j \rangle = \begin{cases} -\frac{1}{2}(\ell + 1) & \text{for } j = \ell - s \\ \frac{1}{2}\ell & \text{for } j = \ell + s \end{cases} \tag{32}$$

which gives $\langle \ell \cdot s \rangle$ is 1/2 for $p_{3/2}$ and -1 for $p_{1/2}$. In the limit of jj coupling, such as for a deep core level, the spin and orbit are aligned,

$$\langle \ell_z \rangle = 2 \langle \ell \cdot s \rangle \langle s_z \rangle, \tag{33}$$

so that $I^{10} = I^{01}$ for $p_{3/2}$ and $I^{10} = -2I^{01}$ for $p_{1/2}$, as can be verified from Fig. 1.

The integrated intensity over each j-level is zero, except for I^{00} and I^{11}, which contain the monopole term, V^0. These spectra are proportional to expectation values of the number of electrons and spin–orbit coupling, respectively. Table 3 shows that the spin–orbit spectrum has a monopole and quadrupole term: $I^{11} = I^{110} + I^{112}$. For the monopole contribution the table shows that $I^{110}_{j=1/2} = -2I^{110}_{j=3/2}$, which is in agreement with Eq. (32). Only $j = 3/2$ can contain a quadrupole moment. The spin–orbit spectra are defined as [38]

$$I^{110} = \frac{\langle \ell \cdot s \rangle}{3\ell s} = \frac{1}{3\ell s} \left[\langle \ell_x \cdot s_x \rangle + \langle \ell_y \cdot s_y \rangle + \langle \ell_z \cdot s_z \rangle \right], \tag{34a}$$

$$\begin{aligned} I^{112} &= \frac{1}{\ell s} \left[\langle \ell_z \cdot s_z \rangle - \frac{1}{3} \langle \ell \cdot s \rangle \right] \\ &= \frac{1}{\ell s} \left[\frac{2}{3} \langle \ell_z \cdot s_z \rangle - \frac{1}{3} \langle \ell_x \cdot s_x \rangle - \frac{1}{3} \langle \ell_y \cdot s_y \rangle \right], \end{aligned} \tag{34b}$$

$$I^{11} = I^{110} + I^{112} = \frac{\langle \ell_z \cdot s_z \rangle}{\ell s}. \tag{34c}$$

Similarly, the anisotropic spin spectrum contains a dipole and octupole term: $I^{21} = I^{211} + I^{213}$.

Finally, we mention that because the fundamental spectra do not contain any geometrical information they can be calculated using an arbitrary order of multipole transition. For an ℓ shell it is convenient to use $Q = \ell$ transitions to the s continuum. Then the fundamental spectra can be obtained using the transformation

$$I^{xy} = A^{Qc\ell}_x \sum_{q\sigma} V^{Qx}_q V^{sy}_\sigma I^{Q}_{q\sigma}. \tag{35}$$

3.4. Multi-electronic configurations

The one-electron model gives a limited description of the experimental photoemission spectra, with only a moderate agreement, even in the case of itinerant metals, such as Fe and Co [39–41]. This provides strong evidence for the presence of correlation effects, which requires a many-electron model. Generally, ψ and ψ' are multi-electron wave functions, i.e., entangled states with core-valence interactions. The transitions can be given by $d^n \to \ell^{-1} d^n c$ or $\ell^n \to \ell^{n-1} c$ for core or valence photoemission, respectively, with expressions for I^{xy} found in Refs. [21] and [22]. The expressions for the rare earth $4f^n$ spectra are relatively simple in LS coupling, where $|\psi\rangle = |\ell^n LSM_L M_S\rangle$ and $|\psi'\rangle = |\ell^{n-1} \underline{LSM_L M_S}\rangle$. Each individual peak in the multiplet structure gives information about the correlation of

the momenta in the corresponding final state $\underline{LSJ}$. The dependence of the spectra on J is complicated but summing over the J components of a term gives a transparent analysis in $\underline{LS}$ coupling. Using Wigner–Racah algebra gives that Eq (21) contains the 6j-symbols

$$\begin{Bmatrix} \ell & x & \ell \\ Q & c & Q \end{Bmatrix} \begin{Bmatrix} L & x & L \\ \ell & \underline{L} & \ell \end{Bmatrix} \begin{Bmatrix} S & y & S \\ s & \underline{S} & s \end{Bmatrix} \propto A_x^{Qc\ell} A_x^{\ell\underline{L}L} A_y^{s\underline{S}S}, \tag{36}$$

with A from Eq. (22) (for details see Eq. (13) in Ref. [22]). The intensities for $\underline{LS}$ peaks in the isotropic spectrum are

$$I^{00}(\underline{LS}) = \frac{1}{6} A_0^\ell A_0^L A_0^S |\langle LS \| \ell^\dagger \| \underline{LS} \rangle|^2, \tag{37}$$

which measures the parentage of the ground state to the final states [42].

In the spin spectrum the $\underline{LS}$ peak intensities are

$$\frac{I^{01}(\underline{LS})}{I^{00}(\underline{LS})} \propto \frac{A_1^{s\underline{S}S}}{A_0^S} \langle S_z \rangle. \tag{38}$$

The coefficient $A_1^{s\underline{S}S}$ gives the alignment of S with the spin s (=1/2) of the hole created and the final states with low spin ($\underline{S} = S - s$) and high spin ($\underline{S} = S + s$) which have intensities proportional to $S+1$ and $-S$, respectively, times $\langle S_z \rangle$.

As an example, the 4f photoemission from rare earth (RE) atoms with $n \leq 6$ shows only low-spin final states; therefore, the spin spectrum is proportional to the isotropic spectrum with all peaks positive [22]. For 4f photoemission from RE $n \geq 7$, the sign of $\langle S_z \rangle$ is reversed, and the low-spin final states have negative intensities, whereas positive intensities are obtained for the high-spin final states with among it the Hund's rule state at the low binding energy side of the spin spectrum [22].

In the orbit spectrum the $\underline{LS}$ peak intensities are

$$\frac{I^{10}(\underline{LS})}{I^{00}(\underline{LS})} \propto \frac{A_1^{Qc\ell} A_1^{\ell\underline{L}L}}{A_0^\ell A_0^L} \langle L_z \rangle. \tag{39}$$

The coefficient $A_1^{\ell\underline{L}L}$ gives the alignment of L with the orbital momentum ℓ of the created hole when they combine to give $\underline{L}$. In LS coupling the dichroism is only determined by the orbital momenta L and $\underline{L}$, where high and low $\underline{L}$ values give peaks with opposite intensities.

In the spin–orbit spectrum the intensities are

$$\frac{I^{11}(\underline{LS})}{I^{00}(\underline{LS})} \propto \frac{A_1^{Qc\ell} A_1^{\ell\underline{L}L} A_1^{s\underline{S}S}}{A_0^\ell A_0^L A_0^S} \langle L_z S_z \rangle. \tag{40}$$

The spin–orbit spectrum I^{11} and orbit spectrum I^{10} are similar in shape for less than half-filled shells. For small spin–orbit interaction we have that $I^{11} = I^{10}(I^{01}/I^{00})$; thus with only low-spin final states I^{11} will be proportional to the I^{10} spectrum. For more than half-filled shells there are larger differences because high- and low-spin states have opposite signs and because the spin–orbit interaction increases along the 4f series. The other fundamental spectra are more complicated and will not be discussed here.

3.5. Coupled tensor operators

For later use we introduce the coupled tensor operators, w^{xyz}, which treat any moment of a shell ℓ with spin–orbit interaction, containing one or more electrons [43]. These tensors are common use in X-ray absorption spectroscopy (XAS) and X-ray magnetic dichroism, where their expectation values can be related to the total intensities using the sum rules, [44–48,38] see Section 7. We shall see in Section 3.6 that these tensors play an equal important role in photoemission. In fact, the photoemission transition $\ell \to c$ can be considered as the particle-hole conjugate of the XAS core to valence transition $c \to \ell$.

The coupled tensor operators for a shell ℓ with orbital, spin and total angular moments, x, y, z, respectively, are defined as

$$w_\zeta^{xyz} \equiv \sum_{\xi\eta} w_{\xi\eta}^{xy} \begin{pmatrix} x & z & y \\ -\xi & \zeta & -\eta \end{pmatrix} (-1)^{x-\xi+y-\eta} n_{xyz}^{-1}, \tag{41}$$

where the LS-coupled operators are

$$w_{\zeta\eta}^{xy} \equiv n_{\ell x}^{-1} n_{sy}^{-1} \sum_{mm'\sigma\sigma'} \ell_{m'\sigma}^\dagger \ell_{m\sigma} (-)^{\ell-m'+s-\sigma'} \times \begin{pmatrix} \ell & x & \ell \\ -m' & \xi & -m \end{pmatrix} \begin{pmatrix} s & y & s \\ -\sigma' & \eta & \sigma \end{pmatrix}, \tag{42}$$

which in SO_2 symmetry simplifies to

$$w^{xyz} = n_{xyz}^{-1} \begin{pmatrix} x & z & y \\ 0 & 0 & 0 \end{pmatrix} \sum_{m\sigma} \ell_{m'\sigma}^\dagger \ell_{m\sigma} V_m^{\ell x} V_\sigma^{sy}. \tag{43}$$

The w^{z0z} with z even describe the shape (i.e., the 2^z-pole) of the charge distribution and the w^{x1z} describe spin–orbit correlations. Moments with $x+y+z$ odd describe axial couplings between spin and orbit, such as $w^{111} = -2\ell^{-1}(\ell \times s)$.

The operators w^{xyz} have a simple relation to the conventional operators O^{xyz},

$$w^{xyz} = \frac{(-1)^z O^{xyz} 2^x (2\ell!) 2^y}{(2\ell - x)!}, \tag{44}$$

their values in SO_2 symmetry are

$$w^{000} = \sum_m \ell_{m\sigma}^\dagger \ell_{m\sigma} = n_\ell, \tag{45a}$$

$$w^{011} = -s^{-1} S_z, \tag{45b}$$

$$w^{101} = -\ell^{-1} L_z, \tag{45c}$$

$$w^{110} = (\ell s)^{-1} \sum_i \ell_i s_i, \tag{45d}$$

$$w^{211} = -\frac{2\ell + 3}{\ell} T_z, \tag{45e}$$

$$w^{202} = \frac{3}{\ell(2\ell - 1)} Q_z \tag{45f}$$

for the number of electrons n_ℓ, spin magnetic moment S_z, orbital magnetic moment L_z, spin–orbit coupling $\ell \cdot s$, magnetic dipole term T_z, and quadrupole moment Q_z, respectively, of the ℓ shell.

Instead of LS-coupled tensors we can define jj-coupled tensors [47], which are also related to integrated intensities using sum rules [48]. The jj-coupled tensors are useful for actinides [49]. Both types of coupled tensors can of course be used in intermediate coupling.

3.6. Integrated spectra and sum rules

The sum rules for photoemission are obtained by extending the set of final states to the whole Hilbert space (states that cannot be reached in the transition do not contribute to the intensity) [50] and then using the closure relation. This yields for the operator part of Eq. (21)

$$\sum_{\psi'} \langle \psi | \ell_{m\sigma}^\dagger | \psi' \rangle \langle \psi' | \ell_{m\sigma} | \psi \rangle = \langle \psi | \ell_{m\sigma}^\dagger \ell_{m\sigma} | \psi \rangle = \langle n_{m\sigma} \rangle. \tag{46}$$

Different from the one-electron state [Eq. (25)], in the case of a general many-electron configuration we sum over the final states $|\psi'\rangle$.

Substituting Eq. (46) in (21) allows us to derive expressions for the integrated intensities, ρ^{xy}, which are given in the last column of Table 1. It can be shown that [26]

$$\rho^{xyz} \equiv \int d\omega\, I^{xyz} \propto A_x^{Qc\ell} \langle w^{xyz} \rangle, \tag{47}$$

where $A_x^{Qc\ell}$, given by Eq. (22), contains the emission channel dependence. For filled core levels, $\langle w^{000} \rangle = n_\ell = 4\ell + 2$, and $\langle w^{xyz \neq 000} \rangle = 0$, which means that the $I^{xyz \neq 000}$ spectra have zero integrated intensity. In the case of partial filled shells, such as the rare-earth 4*f* shell, these sum rules can give useful results.

3.7. Beyond the sum rules: spectral distributions

Apart from the integrated intensity, i.e., the zero-order moment of the spectral distribution, information can be extracted from the higher order moments. The *n*th moment of a spectrum is defined as [51]

$$I^{(n)} \equiv \int_0^\infty d\omega\, \omega^n I(\omega) = \langle \phi | T^\star \mathcal{H}^n T | \phi \rangle. \tag{48}$$

For $n = 0$, we measure $\langle T^\star T \rangle$, which gives the known sum rules for dichroism and spin polarization. For $n = 1$, we obtain new results measuring $\langle T^\star \mathcal{H} T \rangle$. The Hamiltonian $\mathcal{H}$ can contains a set of terms such as Coulomb, exchange and spin–orbit interactions, crystal field and magnetic terms. Knowledge of the first moment is useful for emission from closed shells, where the zero moment (integrated intensity) of the dichroic and spin polarized photoemission spectrum is zero [7,52]. To give a non-trivial example, consider the core-valence interactions between a *p* core level and a *d* valence level, the first moments of the *p* photoemission are [26]

$$I^{00(1)} = \langle n_d \rangle (\frac{2}{5} G^1 + \frac{9}{35} G^3), \tag{49a}$$

$$I^{01(1)} = \langle w_d^{01} \rangle (\frac{2}{5} G^1 + \frac{9}{35} G^3), \tag{49b}$$

$$I^{10(1)} = \langle w_d^{10} \rangle (\frac{2}{5} G^1 - \frac{6}{35} G^3), \tag{49c}$$

$$I^{11(1)} = \langle w_d^{11} \rangle (\frac{2}{5} G^1 - \frac{6}{35} G^3), \tag{49d}$$

with 2*p*-3*d* exchange integrals G^k.

The origin of the first moment in I^{10} can be understood as follows: The final states are split by the exchange interaction such that the states with high (low) orbital moment have on average low (high) final-state energies. So, an electron with its orbital moment parallel to the valence shell will leave the atom with a lower energy than an antiparallel one, shifting the energies of the spectra with left and right circularly polarized light with respect to each other because these produce preferentially photoelectrons of one polarization.

4. Angular dependence

So far we have only dealt with the angle-integrated photoemission, which served to introduce the fundamental spectra. The angular distribution offers additional possibilities. Angular momentum conservation is fulfilled by including the photoelectron angular distribution, which carries away a moment *b*, so that the moments *a* and *x* no longer have to be equal (see Table 5). The transition matrix element

$$T_{q\sigma}^Q(\varepsilon, \mathrm{P_S}) = \sum_{m\gamma} \langle \psi' | \ell_{m\sigma} | \psi \rangle \langle \ell m | C_q^Q | c\gamma \rangle C_\gamma^c(\varepsilon) C_\sigma^s(\mathrm{P_S}) e^{i\delta_c}, \tag{50}$$

Table 5
Possible values for the triad *abx* for the bipolar spherical harmonics U^{abx} in angular dependent photoemission.

Light polarization **P** with moments $a = 0, 1, \ldots, 2Q$.		
$a = 0$	Isotropic	$J^0 = J_{-1} + J_0 + J_1$
$a = 1$	Circular dichroism	$J^1 = -J_1 + J_{-1}$
$a = 2$	Linear dichroism	$J^2 = J_{-1} - 2J_0 + J_1$
Atomic shell ℓ with moments $x = 0, 1, \ldots, 2\ell$.		
$x = 0$	Monopole moment	
$x = 1$	Dipole moment	
$x = 2$	Quadrupole moment	
$x = 3$	Octupole moment	
$x = 4$	Hexadecapole moment	
Photoemission distribution ε with moments $b = \lvert a - x \rvert, \lvert a - x \rvert + 2, \ldots, a + x$.		
$b = 0$	Isotropic emission	
$b = 2$	Quadrupolar part	
etc.		

where

$$C_\kappa^k(\theta, \varphi) \equiv \sqrt{\frac{4\pi}{2k+1}} Y_\kappa^k(\theta, \varphi) \tag{51}$$

is the normalized spherical harmonic and δ_c is the phase of the outgoing electron *c*.

The photoemission J^{ay} in direction ε with spin polarization $\mathbf{P}_S$ and spin moment *y* for light specified by moment *a* and polarization **P** from an atom with multipole moments *x* along **M** is obtained by recoupling as [31]

$$J^{ay}(\mathbf{P}, \varepsilon, \mathrm{P_S}) = \frac{1}{8\pi} \sum_{xz\zeta} n_{xyz}^2 I_\zeta^{xyz} \sum_b U_\zeta^{abxyz}(\mathbf{P}, \varepsilon, \mathrm{P_S}) B_{abx}^{Q\ell}, \tag{52}$$

where

$$B_{abx}^{Q\ell} = \sum_{cc'} A_{abx}^{Qcc'\ell} R^{\ell Qc} R^{\ell Qc'} e^{i\delta} \tag{53}$$

and n_{xyz} is a normalization factor [12]. $R^{\ell Qc}$ is the radial matrix element and $\delta = (\delta_c - \delta_{c'})$ is the phase difference for excitation to the two continuum states, which gives interference between the two final state channels *c* and *c*′. The fundamental spectra I^{xyz}, which we already encountered in Section 3, contain the physical information. Eq. (54) shows that each I^{xyz} produces a limited set of angular distributions U^{abxyz} times the radial matrix elements and phase shifts.

For the simple case of spin-integrated photoemission in SO_2 symmetry, Eq. (52) reduces to

$$J^a(\mathbf{P}, \varepsilon, \mathbf{M}) = \frac{1}{4\pi} \sum_x I^x \sum_b U^{abx}(\mathbf{P}, \varepsilon, \mathbf{M}) B_{abx}^{Q\ell}. \tag{54}$$

The moment $a = 0$ means isotropic light, i.e., the sum of intensities obtained with right-circularly ($q = \Delta m = -1$), *Z*-linearly ($q = \Delta m = 0$) and left-circularly ($q = \Delta m = +1$) polarized radiation. For isotropic light the polarization **P** has no meaning. By $a = 1$ we denote circular dichroism, which is the difference in intensities for left and right circularly polarized light with the helicity vector along **P**. By $a = 2$ we denote linear dichroism: the intensities for light polarized in two perpendicular directions perpendicular to **P** ($q = 1$ and -1) minus twice the intensity for light polarized along **P**.

Table 6
Explicit expressions for the angle dependent functions $U^{abx}(\mathbf{P},\varepsilon,\mathbf{M})$. The last column gives the corresponding spectroscopy.

$U^{000}=1$	
$U^{022}=\frac{3}{2}(\varepsilon\cdot\mathbf{M})^2-\frac{1}{2}$	
$U^{101}=\mathbf{P}\cdot\mathbf{M}$	MCD
$U^{121}=\frac{3}{2}(\mathbf{P}\cdot\varepsilon)(\varepsilon\cdot\mathbf{M})-\frac{1}{2}(\mathbf{P}\cdot\mathbf{M})$	MCD
$U^{122}=\frac{6}{5}(\varepsilon\cdot\mathbf{M})\mathbf{P}\cdot(\varepsilon\times\mathbf{M})$	CDAD
$U^{202}=\frac{3}{2}(\mathbf{P}\cdot\mathbf{M})^2-\frac{1}{2}$	MLD
$U^{220}=\frac{3}{2}(\mathbf{P}\cdot\varepsilon)^2-\frac{1}{2}$	
$U^{221}=\frac{6}{5}(\mathbf{P}\cdot\varepsilon)\mathbf{P}\cdot(\varepsilon\times\mathbf{M})$	MLDAD

4.1. Radial part

We now show the special effects that occur when there is interference. The recoupling coefficient A in Eq. (53) is proportional to a 9j-symbol

$$A^{Qcc'\ell}_{abx}\propto\begin{Bmatrix} Q & a & Q\\ c & b & c'\\ \ell & x & \ell\end{Bmatrix}. \tag{55}$$

Without interference ($c=c'$) the 9j-symbol has two identical columns ($Qc\ell$). For odd permutations its value is multiplied by $(-)^S$, where S is the sum of all nine arguments. Then, since b is even due to parity, the value of a+x has to be even. Hence interference terms ($c\neq c'$) are only allowed for odd values of a+x, and this requires angular functions U^{abx} that are chiral, as we will show in Section 4.2.

For $a+x$ even, the factor $A^{Qcc'\ell}_{abx}$ is real and symmetric in c and c', and for $a+x$ odd, $A^{Qcc'\ell}_{abx}$ is imaginary and antisymmetric in c and c', so that

$$B^{Q\ell}_{abx}=\begin{cases} A^{Qcc'\ell}_{abx}R^cR^{c'}2\cos\delta, & \text{for } a+x \text{ even},\\ A^{Qcc'\ell}_{abx}R^cR^{c'}2i\sin\delta, & \text{for } a+x \text{ odd},\end{cases} \tag{56}$$

where we used $e^{i\delta}+e^{i\delta}=2\cos\delta$ and $e^{i\delta}-e^{i\delta}=2i\sin\delta$.

4.2. Angular functions

The angular functions in Eq. (54) are the bipolar spherical harmonics

$$U^{abx}_0(\mathbf{P},\varepsilon,\mathbf{M})=n^{-1}_{abx}\sum_\alpha\begin{pmatrix} a & b & x\\ -\alpha & \alpha & 0\end{pmatrix}C^a_\alpha(\mathbf{P})C^b_{-\alpha}(\varepsilon)C^x_0(\mathbf{M}) \tag{57}$$

where n_{abx} is a normalization constant [12]. Expressions for some U^{abx} are listed in Table 6 [25].

Eq. (54) can be written in more compact form as a sum over products of physical and angular parts

$$J^a(\mathbf{P},\varepsilon,\mathbf{M})=\sum_{bx}I^xZ_{abx}(\mathbf{P},\varepsilon,\mathbf{M}), \tag{58}$$

where

$$Z_{abx}(\mathbf{P},\varepsilon,\mathbf{M})\equiv\frac{1}{4\pi}U^{abx}(\mathbf{P},\varepsilon,\mathbf{M})B_{abx}. \tag{59}$$

Table 7 gives a quick reference to the photoemission expression for $Q=1$. For instance, p emission (where $x\leq 2$) gives

$$J^0=I^0Z_{000}+I^2Z_{022}, \tag{60a}$$

$$J^1=I^1(Z_{101}+Z_{121})+I^2Z_{\mathbf{122}}, \tag{60b}$$

$$J^2=I^0Z_{220}+I^1Z_{\mathbf{221}}+I^2(Z_{202}+Z_{222}+Z_{242}). \tag{60c}$$

In angle integrated emission ($b=0$) we have $x=a$, so that the circular dichroism J^1 gives the I^1 spectrum and the linear dichroism J^2 gives the I^2 spectrum. The moment $b=2$ corresponds to a quadrupolar distribution. This allows to measure I^1 either in circular dichroism (abx = 121) or in linear dichroism (abx = 221). Likewise, I^2 can be measured either in circular (abx = 221) or in linear dichroism (abx = 2b2). See Table 8 for a summary, where the chiral geometries ($a+x$ is odd) are bold printed.

Table 7
Quick reference to the photoemission expression $J^a=\sum_{bx}I^xZ_{abx}$ for $Q=1$. Odd values of $a+z$ are printed bold faced in Z_{abx} and give interference terms between $c=\ell-1$ and $c=\ell+1$ in CDAD ($a=1$) and MLDAD ($a=2$).

	J^0	J^1	J^2
I^0	Z_{000}	–	Z_{220}
I^1	–	$Z_{101}+Z_{121}$	$Z_{\mathbf{221}}$
I^2	Z_{022}	$Z_{\mathbf{122}}$	$Z_{202}+Z_{222}+Z_{242}$
I^3	–	$Z_{123}+Z_{143}$	$Z_{\mathbf{223}}+Z_{\mathbf{243}}$
I^4	Z_{044}	$Z_{\mathbf{144}}$	$Z_{224}+Z_{244}+Z_{264}$
I^5	–	$Z_{145}+Z_{165}$	$Z_{\mathbf{245}}+Z_{\mathbf{265}}$
I^6	Z_{066}	$Z_{\mathbf{166}}$	$Z_{246}+Z_{266}+Z_{286}$

Table 8
The different geometries with their spectra, symmetry properties and angle dependent factors for p emission. Odd values of $a+x$ are printed in bold face.

Acronym	J^a	I^x	$a+x$	Z_{abx}
MCD	J^1	I^1	Even	$Z_{101}+Z_{121}$
CDAD	J^1	I^2	Odd	$Z_{\mathbf{122}}$
MLDAD	J^2	I^1	Odd	$Z_{\mathbf{221}}$
LD	J^2	I^2	Even	$Z_{202}+Z_{222}+Z_{242}$

5. Geometrical aspects

The waves with $a+x$ is odd can only be measured when $\mathbf{P}$, ε, and $\mathbf{M}$ are neither coplanar nor mutually perpendicular. U^{abx} changes sign whenever one of the vectors corresponding to an odd moment a or x is inverted. The intensity of an odd wave with two even moments is zero when one of the even moments is perpendicular to the other two moments. This is because inversion of the odd moment, which gives a sign change, followed by a rotation leads to the same geometry as inversion of the two even moments, which gives no sign change.

The total-symmetric spherical functions U are invariant for inversion. This restricts the possible values of the moments and gives rise to the following rules: [31]

Rule A. If all vectors are coplanar, the sum of all moments must be even.

Rule B. If a vector is perpendicular to a plane containing the other vectors, the sum of the latter vectors must be even.

Rule C. If there are three mutually perpendicular sets of collinear vectors, all three sets must have the same parity (i.e., either even or odd).

5.1. Coplanar geometry

To illustrate the above symmetry rules we consider the emission from a p shell. The four basic geometries for spin-integrated photoemission are listed in Table 8.

5.1.1. MCD

The p shell emission is given as

$$J_{\mathrm{MCD}}=\frac{1}{12\pi}I^1\{\mathbf{P}\cdot\mathbf{M}(R_s^2-R_d^2)+[3(\mathbf{P}\cdot\varepsilon)(\varepsilon\cdot\mathbf{M})-\mathbf{P}\cdot\mathbf{M}]\times(R_d^2-R_sR_d\cos\delta)\}. \tag{61}$$

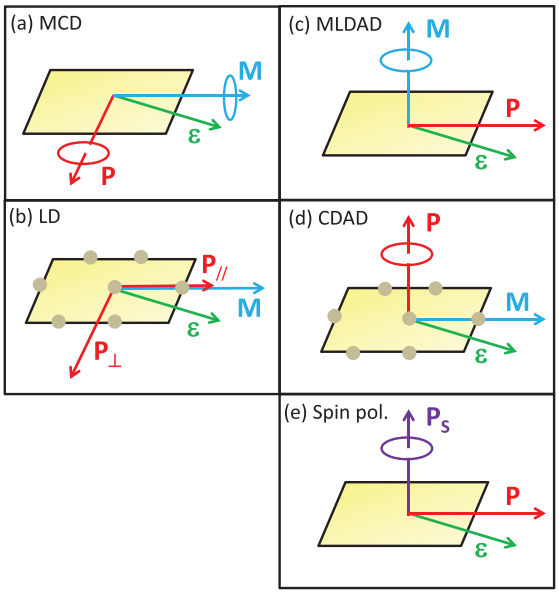

Fig. 2. Geometries of (a) MCD, (b) LD, (c) MLDAD, (d) CDAD, and (e) spin polarization. Vectors with a circle are odd, while the others are even.

The MCD signal is proportional to the orbit spectrum. The first term gives the angle integrated part which depends only on the angle (**P**,**M**) and the squared radial matrix elements for transition to the εs and εd continua. The second term gives the angular dependence which, apart from the squared radial matrix element to the εd continuum, contains the interference term between the εs and εd channels with a phase difference δ. This interference term, which can become the dominant term at certain emission directions, has been omitted in early experimental studies [6]. The geometry, shown in Fig. 2(a), can be chosen with all vectors in plane, so that chiral effects vanish. Since **P** ($a=1$) and **M** ($x=1$) are odd, and ε ($b=0, 2$) is even, the sum of the vectors in the plane is even (Rule A). No circular dichroism is observed for in-plane **M** is even ($x=0$, 2).

5.1.2. LD

Even moments of **M**, including those induced by a crystalline field, can be measured in linear dichroism (LD) as is shown in Fig. 2(b). $J_{\rm LD} \propto I^2$, thus $\mathbf{P}_\perp - \mathbf{P}_\parallel$ measures the quadrupole moment of the p shell.

5.2. Chiral geometry

5.2.1. MLDAD

In a geometry without inversion symmetry (i.e., **P**, ε, **M** are neither coplanar nor mutually perpendicular) the orbit spectrum I^1 can be measured using linearly polarized light. Since for linear polarization the vector **P** is even, the part of the transition probability containing R_s^2 and R_d^2 remain unchanged upon reversal of **M**, so that in the difference spectrum the contributions to the εs and εd continua cancel. However, reversal of **M** changes the factor $R_sR_d\,e^{i\delta}$ in the interference term into $R_sR_d\,e^{-i\delta}$, resulting in a dichroic signal

$$J_{\rm MLDAD} = \frac{3}{4\pi} I^1\,(\mathbf{P}\cdot\varepsilon)\,\mathbf{M}\cdot(\mathbf{P}\times\varepsilon) R_sR_d \sin\delta. \tag{62}$$

The vector product shows that the MLDAD vanishes for $\varepsilon \perp \mathbf{P}$ and $\varepsilon \parallel \mathbf{P}$, which is in agreement with Rule C.

Taking $\pm\mathbf{M} \parallel z$, $\mathbf{P} \parallel x$, $\varepsilon(\theta, \phi)$ gives an angular distribution $\sin^2\theta \sin 2\phi$. Thus the maximum signal is obtained for $\theta = 90^\circ$ and $\phi = 45^\circ$ or 135°. The signal has opposite sign for ϕ and $-\phi$. Integrated over all angles the signal is zero. The measurement geometry is displayed in Fig. 2(c), where we can verify Rule A by observing that the sum of the vectors **P** ($a=2$) and ε ($b=2$), in the plane perpendicular to **M**, is even. Plots of the angular distribution can be found in Ref. [25].

The measured MLDAD in Gd $4f^7$ photoemission has been analyzed in Refs. [53,54].

Table 9
Character table of the group $D_2 = C_2 \times C_2$. Symmetric (even) and antisymmetric (odd) functions with respect to {M,P} are indicated by 1 and −1, respectively. E is the identity operator. The irreducible representations Γ_n correspond to the various spectra, which are forming independent linear combinations.

	E	M	P	M·P	spectrum
Γ_1	1	1	1	1	SUM
Γ_2	1	−1	−1	1	MCD
Γ_3	1	1	−1	−1	CDAD
Γ_4	1	−1	1	−1	MLDAD

5.2.2. CDAD

The behaviour of CDAD (= I^2Z_{122}) is similar to that of MLDAD (= I^1Z_{221}). If we interchange the labels of the vectors **M** and **P** the geometry (c) in Fig. 2 goes over into (d). Now **M** ($x=2$) is even and **P** ($a=1$) is odd. The CDAD can be expressed as

$$J_{\rm CDAD} = \frac{1}{4\pi} I^2\,(\mathbf{M}\cdot\varepsilon)\,\mathbf{P}\cdot(\varepsilon\times\mathbf{M}) R_sR_d \sin\delta, \tag{63}$$

where we used $\mathbf{M}\cdot(\mathbf{P}\times\varepsilon) = \mathbf{P}\cdot(\varepsilon\times\mathbf{M})$. CDAD is measured by reversing **P**. The signal vanishes for $\varepsilon \perp \mathbf{M}$ and $\varepsilon \parallel \mathbf{M}$.

5.2.3. SPAD

The transverse geometry also serves to measure the spin–orbit spectrum I^{11} in spin polarized photoemission. Rule C is obeyed, and we simply replace the vector **M** ($x=1$) by the vector $\mathbf{P}_S$ ($y=1$) in Fig. 2 to obtain geometry (e) from (c). The spin polarization in the angular dependence is

$$J_{\rm SPAD} = \frac{1}{4\pi} I^{11}\,(\mathbf{P}\cdot\varepsilon)\,\mathbf{P}_S\cdot(\mathbf{P}\times\varepsilon) R_sR_d \sin\delta. \tag{64}$$

The spin polarization in linearly dichroism has been measured in Cu $3p$ photoemission [55].

5.3. A group theoretical viewpoint

Further insight can be gained by evoking group theory. As should be clear by now, reversing P and M corresponds to the following spectra

$$\begin{aligned}
&P^+M^+ + P^+M^- + P^-M^+ + P^-M^- \cong \text{SUM},\\
&P^+M^+ + P^+M^- - P^-M^+ - P^-M^- \cong 2\,\text{CDAD},\\
&P^+M^+ - P^+M^- + P^-M^+ - P^-M^- \cong 2\,\text{MLDAD},\\
&P^+M^+ - P^+M^- - P^-M^+ + P^-M^- \cong 2\,\text{MCD},
\end{aligned}$$

where $\pm$ indicates an alignment in positive or negative direction. This can be rearranged as

$$\begin{aligned}
&(P^+ + P^-)(M^+ + M^-) \cong \text{SUM},\\
&(P^+ - P^-)(M^+ + M^-) \cong 2\,\text{CDAD},\\
&(P^+ + P^-)(M^+ - M^-) \cong 2\,\text{MLDAD},\\
&(P^+ - P^-)(M^+ - M^-) \cong 2\,\text{MCD},
\end{aligned} \tag{65}$$

which gives symmetric (even) and antisymmetric (odd) functions in P and M. By symmetry, the different spectra correspond to the irreducible representations of the group $D_2 = C_2 \times C_2$, for which the character table is shown in Table 9 [56]. Even and odd functions are indicated by 1 and −1, respectively.

The MCD is given as the difference between the spectra with M and P parallel and antiparallel, respectively. Therefore, it is odd in both P and M, but obviously even in P·M. The MLDAD is the difference between the spectra with opposite directions of M summed over both helicity directions, so that the spectrum is even in P, and hence can be measured using linear polarization. The CDAD is the difference between the spectra with opposite helicity vectors summed over both magnetization directions, so that the spectrum is even in M.

The irreducible representations in Table 9 demonstrate the orthogonality of the four spectra. One can perform a 'complete' experiment by reversing P and/or M to separate the different dichroic spectra. The orthogonality of the functions also provides a method to perform an accurate error analysis [40,41].

6. Crystal field symmetry

The photoemission intensity can be obtained in arbitrary symmetry. In a crystal field with point-group symmetry G there is a spectrum for every totally symmetric function [12]. We can expand the G symmetry functions $|x\Gamma\kappa\rangle$ into spherical harmonics $|x\xi\rangle$ [57]

$$|x\Gamma\kappa\rangle = \sum_{\xi} |x\xi\rangle\langle x\xi|z\Gamma\kappa\rangle, \tag{66}$$

which defines the new linear combinations of spectra and angle dependencies

$$I^x_{\Gamma\kappa} = \sum_{\xi} I^x_{\xi}\langle x\xi|x\Gamma\kappa\rangle, \tag{67}$$

$$V^x_{\Gamma\kappa} = \sum_{\xi} V^x_{\xi}\langle x\Gamma\kappa|x\xi\rangle, \tag{68}$$

and rewrites the intensity as

$$J = \sum_{x\Gamma\kappa} I^x_{\Gamma\kappa} V^x_{\Gamma\kappa} \tag{69}$$

where the irreducible representation has to be totally symmetric, $\Gamma\kappa = A_1$ [58].

7. X-ray absorption and core hole polarization

7.1. X-ray absorption

A brief comparison with XAS is on order. The integrated intensities ρ_q for q-polarized light are obtained for SO_2 symmetry by taking the core to valence transition intensity ($c \rightarrow \ell$) and summing over the final states f and components γ of c,

$$\begin{aligned}\rho_q &= \sum_{f\gamma m\sigma} \langle g|\ell_{m\sigma} c^{\dagger}_{\gamma\sigma}|f\rangle\langle f|\ell^{\dagger}_{m\sigma} c_{\gamma\sigma}|g\rangle \begin{pmatrix} \ell & Q & c \\ -m & q & \gamma \end{pmatrix}^2 \\ &= \sum_{m\sigma} \langle n_{m\sigma}\rangle \begin{pmatrix} \ell & Q & c \\ -m & q & \gamma \end{pmatrix}^2,\end{aligned} \tag{70}$$

where we used the completeness relation. We define the integrated intensities ρ^x of the fundamental spectra as linear combinations of ρ_q,

$$\rho^x = \sum_q V^{Qx}_q \rho_q. \tag{71}$$

Substitution of Eq. (70) into (71) and recoupling using YLV4 [Eq. (20)] with coefficient A_x [Eq. (22)] gives the orbital sum rules for XAS [44,45]

$$\rho^x = A^{Qc\ell}_x \langle \underline{w}^x_{\ell}\rangle. \tag{72}$$

Actually, the core level is split into j level and we find intensities as

$$\rho^z_j \propto \sum_{xy} \langle \underline{w}^{xyz}_{\ell}\rangle. \tag{73}$$

Here, $\underline{w}^{xyz}_{\ell}$ are tensor operators for holes in the valence shell ℓ, for which $\langle \underline{w}^{xyz}\rangle = -\langle w^{xyz}\rangle$ for $xyz \neq 000$, while $\langle \underline{w}^{000}\rangle + \langle w^{000}\rangle = 4\ell + 2$.

7.2. Core hole polarization

The sum rules in XAS, XMCD, and XMLD measure the *number of core holes* (monopole moment) created, but give no information about the polarization of the core hole, which is contained in its higher multipole moments.

The moments r of the spin–orbit split core hole j are defined in the usual way with expectation values describing the core hole polarization

$$\langle w^r_j\rangle = \sum_{m_j} \langle n_{m_j}\rangle V^{jr}_{m_j}. \tag{74}$$

This gives a set of orthogonal operators containing m_j to the power r (with $r = 0, 1, \ldots, 2j$)

$$\langle w^0_j\rangle = \sum_{m_j} \langle n_{m_j}\rangle = \langle n_j\rangle, \tag{75a}$$

$$\langle w^1_j\rangle = \sum_{m_j} \langle n_{m_j}\rangle \frac{m_j}{j} = \frac{\langle J_z\rangle}{j}, \tag{75b}$$

$$\langle w^2_j\rangle = \sum_{m_j} \langle n_{m_j}\rangle \frac{3m_j^2 - j(j+1)}{j(2j-1)} = \frac{\langle 3J_z^2 - J^2\rangle}{j(2j-1)}, \tag{75c}$$

etc. If desired, the $\langle w^z_j\rangle$ moments can be written as a sum over $\langle w^{xyz}\rangle$ moments by using recoupling transforms [47].

The core hole polarization shows up in the line shape (spectral moments) of the XAS, XMCD and XMLD [51]. Conversely, the spectral shape can be obtained by adding the separate contributions from each of the ground state moments. [59–61]

The core hole polarization is also measured by the fundamental spectra in photoemission (cf. Table 3). Integrating the photoemission over the energy, the higher moments average out, and only the monopole moment remains. The core hole polarization can also be measured using resonant photoemission, as shown in the next section [23,31].

8. Resonant photoemission

After XAS, the core hole decays under emission of electrons and photons, as measured by resonant photoemission (RESPES) and resonant inelastic X-ray scattering (RIXS), respectively. For 3d metals this second-order process is given using multi-electronic configurations as

$$3d^n + h\nu \rightarrow 2p^5 3d^{n+1} \rightarrow \begin{cases} 3p^4 3d^{n+1} + \varepsilon & \text{RESPES} \\ 3s^1 3d^{n+1} + h\nu' & \text{RIXS} \end{cases}$$

We shall describe resonant photoemission as a two-step process. The first step is X-ray absorption, which results in a polarized core hole and an additional valence electron. In the second step the core

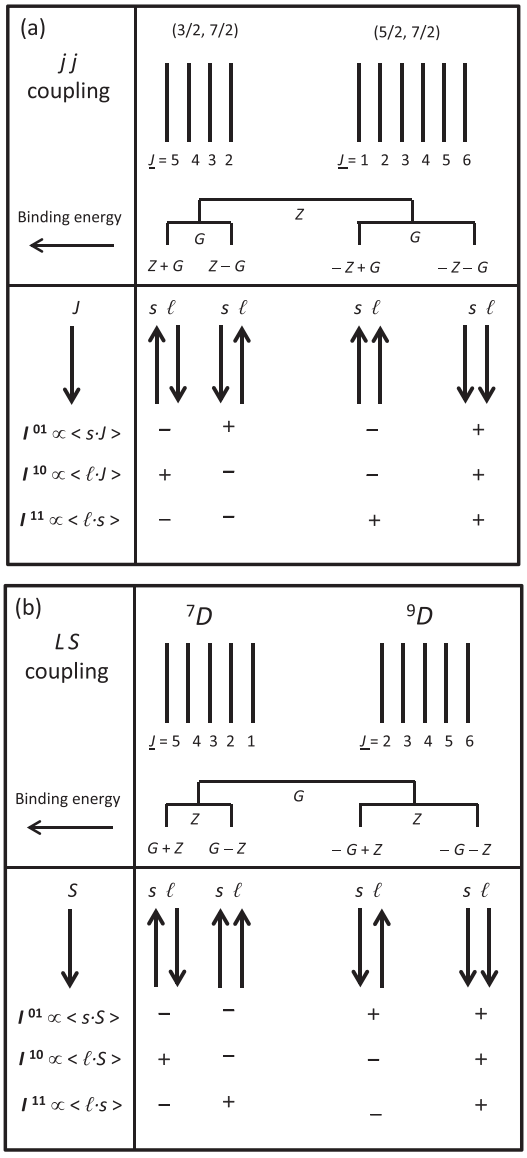

Fig. 3. Correlations between the moments and the shape of the fundamentals spectra for $f^7(J) \rightarrow d^9f^7(J)$ photoemission. (ℓ, s and j are the orbital, spin and total moments of the core hole.) (a) Alignment of moments J, s and ℓ in the jj-coupling limit. (b) Alignment of moments S, s and ℓ in the LSJ coupling limit.

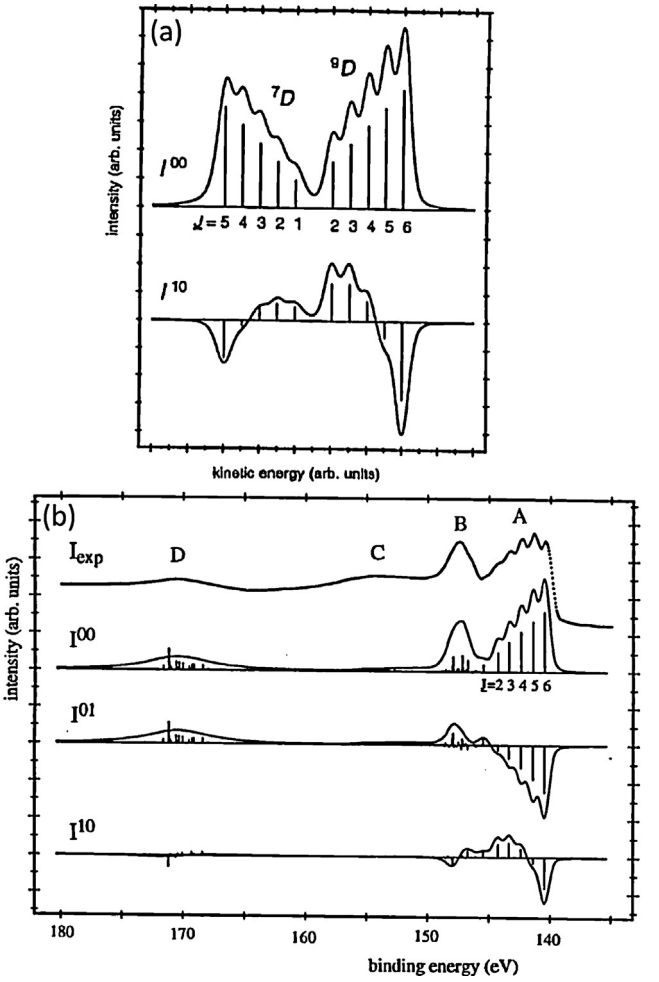

Fig. 4. (a) The spectra I^{00} and I^{10} for d photoemission for the pure ^7D and ^9D states in LSJ coupling. (b) Gd 4d photoemission spectra calculated in intermediate coupling, and experimental data.

hole created decays by Coulomb interaction under emission of a photoelectron and the creation of a two-hole state.

Core hole polarization measurements have been performed on ferromagnetic 3d transition metals [62,63]. The resonant photoemission decay after 2p absorption shows a circular dichroism of ~10% in a geometry where the dichroism in the X-ray absorption is forbidden, i.e., with the magnetization direction perpendicular to the helicity vector of the light. Qualitatively the effect can be understood as follows: XAS with light circularly polarized along **P** gives an alignment of the core hole orbital moment. However, the spin–orbit interaction in the core hole state tries to align the orbital moment of the core hole parallel to its spin direction along **M**. As a result the orbital moment of the core hole will be aligned in a manner that accommodates both the light polarization and the spin direction. Thus the oriented hole rotates in a plane bisecting **P** and **M**, so that it will have a non-spherical charge distribution, i.e., a quadrupole moment. [64]

Resonant photoemission has the fundamental spectra

$$J^{ah}_{\alpha\nu} = \sum_{qq'\sigma\sigma'} V^{Qa}_{q'q} V^{sh}_{\sigma'\sigma\alpha} J_{q'\sigma'q\sigma\nu}. \tag{76}$$

The angle and spin dependent emission intensity J^{ah}_j from a core state with total angular momentum j to the LS term of the two-core-hole state with SO_2 symmetry using polarized light of moment a and with photoelectron spin of moment h can be written for dipole transitions as [23,31,65]

$$J^{ah}_j(LS; \mathbf{MP}\mathrm{P_S}\varepsilon) = \frac{1}{4\pi} \sum_{zrb} \left\{ \sum_{xy} \langle \underline{w}^{xyz}_0 \rangle C^{xyzar}_j \right\} \times U^{zarhb}_0(\mathbf{MP}\mathrm{P_S}\varepsilon) B^{rhb}_j(LS). \tag{77}$$

The angle dependence is given by the multipolar spherical harmonics $U^{zarhb}_0(\mathbf{MP}\mathrm{P_S}\varepsilon)$. The coefficient C^{xyzar}_j gives the transition probability for a state with moment xyz to create a core hole with angular momentum j and moment r. The coefficient $B^{rhb}_j(LS)$, which contains the radial matrix elements, gives the probability for a core hole with moment r to decay into the state LS and a photoelectron emission distribution moment b and spin moment h.

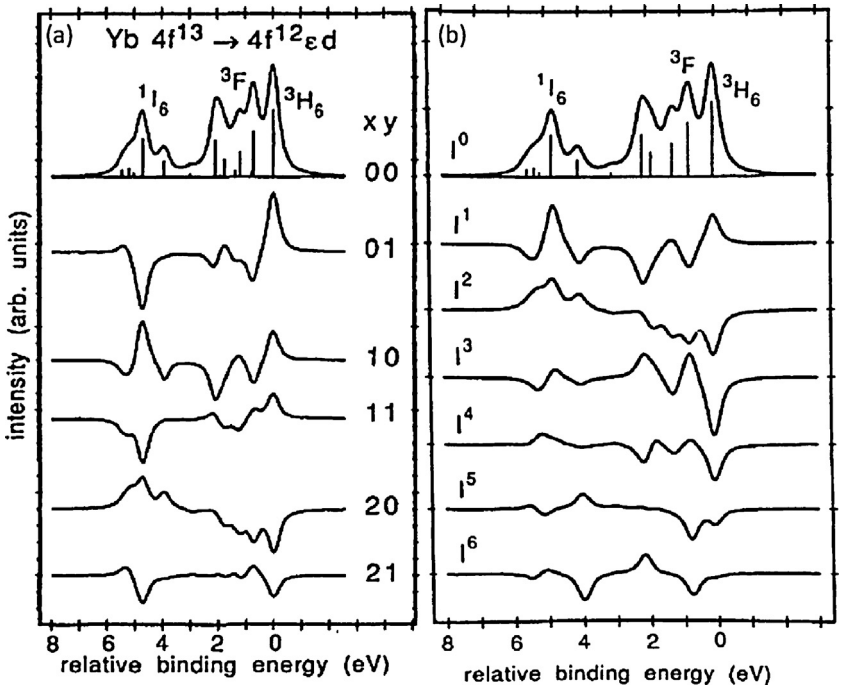

Fig. 5. (a) The fundamental spectra I^{xy} for the photoemission Yb $4f^{13} \rightarrow 4f^{12}\varepsilon d$ calculated using Cowan's code. (b) The fundamental spectra I^{x0} for angle dependent photoemission. All spectra are on the same scale.

In Eq. (77) the resonant photoemission is taken as a two-step process, starting with an excitation from a core level to the valence shell, after which the core hole decays to two shallower core holes while an electron is emitted. The two core holes form well defined states which can be selected by the energy of the emitted electron. The non-spherical core hole and the selected final state cause a specific angle and spin distribution of the emitted electron. The experiment is characterized by the magnetic and non-magnetic moments being measured, the polarization and direction of the light and the spin and angular distribution of the emitted electron. The intensity is a sum over ground state expectation values of tensor operators multiplied by the probability of creating a polarized core hole using polarized light multiplied by the probability for decay of such a core hole into the final state. Using Wigner–Racah algebra [34] we can derive general expressions for the angle and spin dependent intensity in various regimes of Coulomb and spin–orbit interaction, *LS*, *LSJ* and *jjJ* coupling [31].

Writing out $J^1_j(\mathbf{P}, \varepsilon, \mathbf{M})$ for the $2p$ decay gives the integrated intensities [66]

$$4\pi J^1_{3/2} = \left[\langle L_z\rangle + \frac{2}{3}\langle S_z\rangle + \frac{7}{3}\langle T_z\rangle\right](\mathbf{M}\cdot\mathbf{P})B^0 + \left[\frac{1}{10}\langle L_z\rangle + \frac{2}{3}\langle S_z\rangle + \frac{7}{30}\langle T_z\rangle\right][3(\mathbf{M}\cdot\varepsilon)(\varepsilon\cdot\mathbf{M}) - \mathbf{M}\cdot\mathbf{P}]B^2, \quad (78)$$

$$4\pi J^1_{1/2} = \left[\frac{1}{2}\langle L_z\rangle - \frac{2}{3}\langle S_z\rangle - \frac{7}{3}\langle T_z\rangle\right](\mathbf{M}\cdot\mathbf{P})B^0. \quad (79)$$

The XMCD sum rules for the orbital and spin moments can be retrieved using the monopole contributions (B^0) of the sum, $J^1_{3/2} + J^1_{1/2}$, and the weighted difference, $J^1_{3/2} - 2J^1_{1/2}$, respectively.

The $r=0$ and $r=2$ term in $J^1_{3/2}$ give different linear combinations of the operator values $\langle L_z\rangle$, $\langle S_z\rangle$ and $\langle T_z\rangle$. The ratio $\langle L_z\rangle$: $\langle T_z\rangle$ is independent of the geometry, but the ratio $\langle S_z\rangle$: $\langle T_z\rangle$ is 10× larger for $r=2$ than for $r=0$. This offers the possibility to separate the spin magnetization from the magnetic dipole term by varying the angles between **P**, ε and **M**. In a transverse geometry (**P** ⊥ **M**), the $r=0$ term in J^1 disappears, leaving only the $r=2$ term, which facilitates the analysis [62,67,68].

9. Illustrations

9.1. Correlations between the spin and orbital momenta

We shall give a practical example to demonstrate some of the information contained in the fundamental spectra regarding the correlation between spin and orbital moments for the case of Gd $4d$ photoemission [69–71].

9.1.1. Spin–orbit and electrostatic interaction

The Gd atom has an electronic configuration $4f^7 5d^1 6s^2$, where the interaction of the $4f$ with the $5d$ and $6s$ is small, so that we will neglect the $5d6s$. The ground state is dominantly $^8S_{7/2}$ state. The other *LS* states are well separated in energy due to the large Coulomb interaction [$F^2(4f, 4f)$ = 14.5 eV], and the spin–orbit interaction [$\zeta(4f)$ = 0.19 eV] mixes only about two percent ^6P into the ground state.

The final state is $d^9 f^7 c$, where d^9 is the ionised core shell and c the continuum state with no interactions. The relative size of the core-valence interactions and core spin–orbit parameter determines the degree of intermediate coupling in the final state. For deep core levels, such as the Gd $3d$, the spin–orbit parameter is larger than the exchange integral [$\zeta(3d)$ = 12.6 eV and $G^1(3d, 4f)$ = 7.5 eV] which makes it closer to the *jj* coupling limit. Shallower core levels, such as the Gd $4d$ and $5p$, where the electrostatic interaction larger than the spin–orbit interaction [$G^1(4d, 4f)$ = 20.1 eV and $\zeta(4d)$ = 2.2 eV] are closer to the *LS* coupling limit. Although the computation in intermediate coupling is easily performed, making the simplification to *jj* or *LS* coupling is useful to find the approximate assignment of the peak structures and allows for a better understanding of the spectral line shape. The Gd $4d$ core level is of interest because the influence of the electrostatic and spin–orbit interaction can be clearly distinguished from each other. These interactions differ

roughly by an order of magnitude, so that the spin–orbit interaction can be treated as a perturbation.

We will denote the orbital, spin and angular moments of the f^7 and d^9f^7 configurations by LSJ and $\underline{LSJ}$, respectively, and the moments of the core d hole by ℓ, s and j. For Gd $4f^7$ with its half-filled shell, $L = 0$, so that $J = S$ and $\underline{L} = \ell$.

9.1.2. *The* jj*-coupling limit*

We start by evaluating the spectrum in the limit of *jj* coupling. The spin–orbit interaction splits the core state into $d_{5/2}$ and $d_{3/2}$ levels with an energy separation of $\frac{5}{2}\zeta(3d) \approx 30$ eV or $\frac{5}{2}\zeta(4d) \approx 5.5$ eV. For convenience we will take for J the momentum of the $4f$ holes rather than that of the $4f$ electrons.

At the $d_{5/2}$ edge the $j = 5/2$ hole couples with the $J = 7/2$ state of the f^7 to a manifold $\underline{J} = 6, 5, 4, 3, 2, 1$, where the energy spread is determined the exchange interaction G. In the $d_{5/2}$ level the spin and orbit are parallel. The level $\underline{J} = 6$, where s is parallel to J, has the lowest binding energy due to the exchange interaction. This situation is depicted in Fig. 3(a). The coupling condition implies that $\underline{J} = J + j = J + s + \ell$.

At the $d_{3/2}$ edge, with ℓ and s antiparallel, the $J = 7/2$ state of the f^7 state couples to a manifold $\underline{J} = 2, 3, 4, 5$. The level $\underline{J} = 2$, where s is parallel to J, has the lowest binding energy. Thus in the $d_{3/2}$ level the $\underline{J}$ values increase with binding energy, which is opposite as for the $d_{5/2}$ level. The correlation between the moments of J, s and ℓ determine the sign of the fundamental spectra. The spin spectrum gives the correlation of the core spin with the total magnetic moment, i.e., $I^{01} \propto \langle s \cdot J \rangle$. The magnetic dichroism gives the correlation between ℓ and the total magnetic moment, i.e., $I^{10} \propto \langle \ell \cdot J \rangle$. Hence, the alternative name *orbit spectrum*, which is more correct than the term *circular dichroism* since I^{10} can also be measured in linear dichroism using a chiral geometry. The spin–orbit spectrum measures the correlation between ℓ and s, thus $I^{11} \propto \langle \ell \cdot s \rangle$.

The signs of the spectral structure are directly seen from Fig. 3(a). The spin spectrum is positive when the core spin s is parallel with the magnetic moment J and negative when it is antiparallel. This can be understood from the selection rule $\Delta S = 0$ which implies that the spin of the photoelectron is equal to that of the core electron before excitation.

Fig. 3(a) shows that the signal of the orbit spectrum is positive when the core-hole orbit ℓ is parallel to the magnetic moment, which is the case at the high binding energy side of the $d_{5/2}$ level and at the low binding energy side of the $d_{3/2}$ level. The signal is reversed at the opposite side of each j level. The spin–orbit spectrum, I^{11}, which is defined by the difference between the orbit spectra for spin up and spin down emission, shows a positive signal at the $d_{5/2}$ level where ℓ and s are parallel, and a negative signal at the $d_{3/2}$ edge where ℓ and s are antiparallel.

9.1.3. *The* LS*-coupling limit*

With dominant Coulomb and exchange interactions, the angular momentum coupling for the Gd $4d$ photoemission is best approached from the *LS*-coupling limit. From the $f^7(^8S)$ initial state electric-dipole transitions are allowed to the ^9D and ^7D states of the final state configuration d^9f^7. The ^9D state, where the spin is stretched to its maximum value, can only be formed by coupling the $d^9(^2D)$ to the $f^7(^8S)$ state. However, the ^7D state can be formed by coupling the ^2D with either the ^8S, ^6P, ^6D, ^6F or ^6G parent state of the f^7 configuration. These five ^7D states are different angular functions which means they have different electrostatic interactions. Their eigenvalues are found by diagonalization of the energy matrix including the Coulomb and exchange integrals. This results in peaks with an energy spread of ~30 eV. The photoemission intensities of the septet states are given by the square of the coefficients of the ^8S contribution in the ^7D eigenvectors.

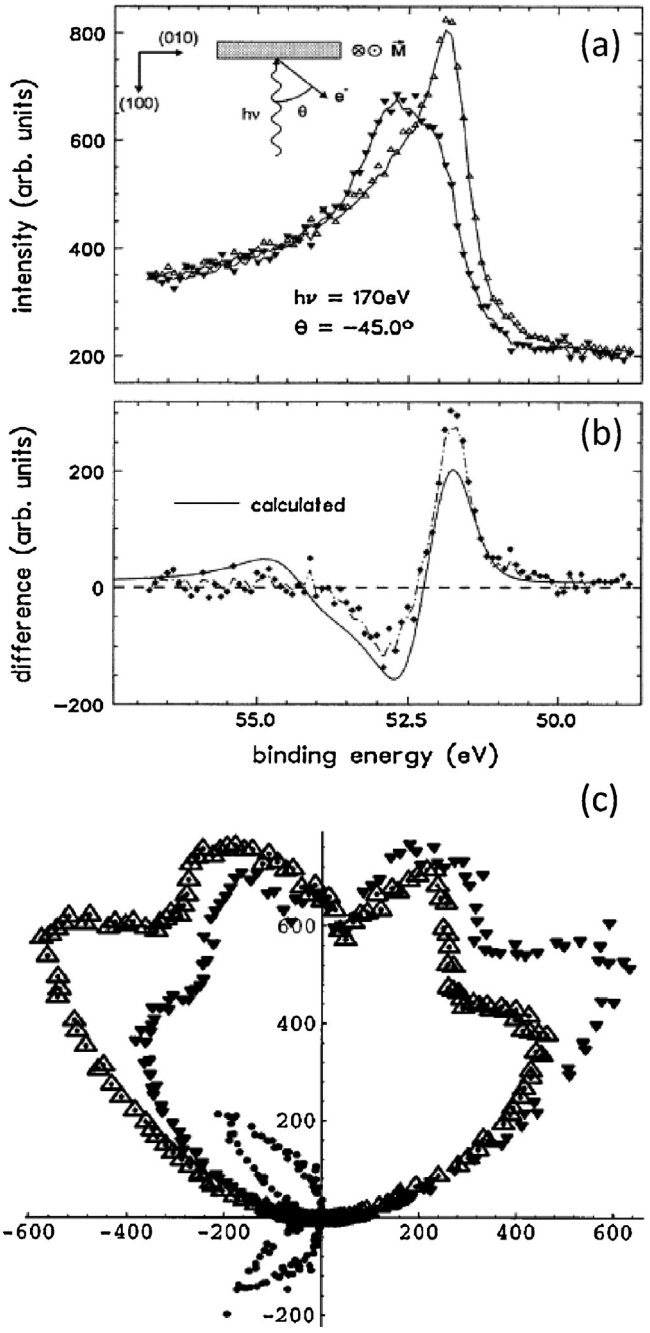

Fig. 6. Experimental MLDAD in Fe $3p$ photoemission of Fe/Ag(100) for geometry shown in inset: **P** and ε (= −45°) are in the plane of the drawing, **M** is perpendicular to the plane of the drawing. Open and closed triangles correspond to magnetization up and down, respectively. (b) The difference spectrum compared to the calculated results from Ref. [25] (c) The Fe $3p$ photoemission at a photon energy of 170 eV and a kinetic energy of 118 eV as a function of emission angle for magnetization up and down. Normal emission is at 0°. The difference spectrum, MLDAD (dots) [27,74].

9.1.4. *First-order spin–orbit interaction*

We will now consider the influence of the first-order spin–orbit interaction in the *LS* states. For small spin–orbit interaction the ^9D state splits into levels $\underline{J} = 6, 5, 4, 3, 2$ and the ^7D state splits into $\underline{J} = 1, 2, 3, 4, 5$ [Fig. 3(b)]. For the moment we will assume that there is only a single low-spin state.

The generic shape of the fundamental spectra is obtained from the correlation between the angular momenta with respect to S, the magnetic moment of the $4f$ holes. Fig. 3(b) shows the coupling between S, s and ℓ for the various levels. The core spin s is coupled

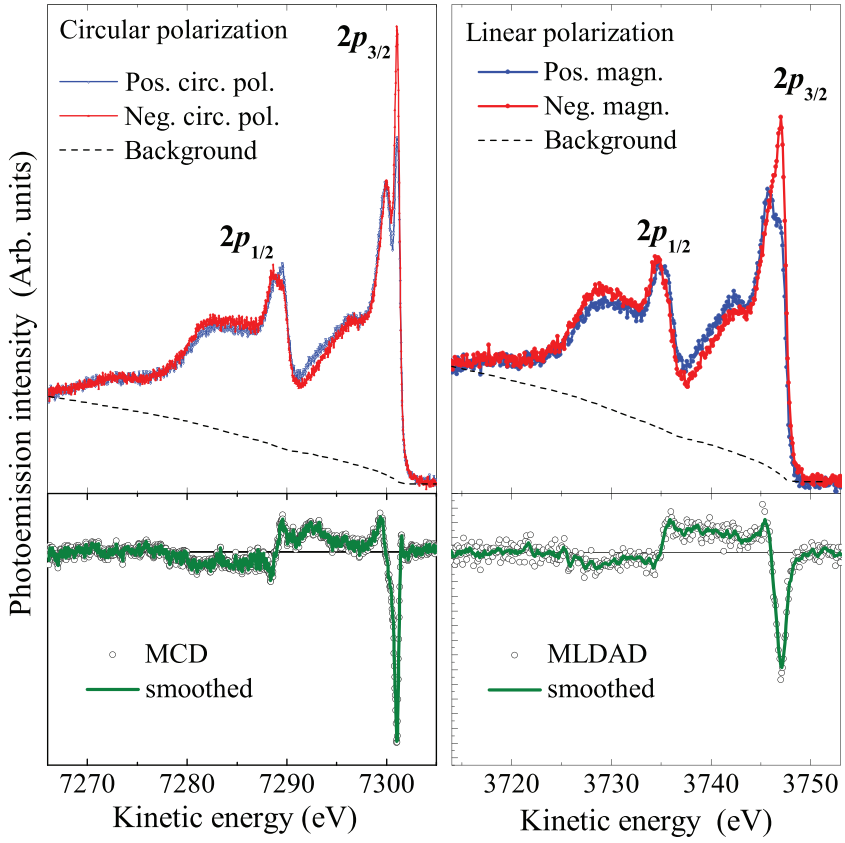

Fig. 7. Mn 2*p* HAXPES from (Ga,Mn)As below T_C. (a) Magnetic circular dichroism (MCD) measured with left and right circularly polarized X-rays at ~7300 eV kinetic energy [75]. (b) Magnetic linear dichroism in angular dependence (MLDAD) measured with linear polarization in opposite chiral geometries, by reversing the magnetization at ~3000 eV kinetic energy [76]. The bottom panels show the difference spectra.

to S by an effective exchange interaction G, resulting in the separation into nonet and septet state, and coupled to ℓ by an effective spin–orbit interaction Z, giving the splitting into J levels. Since $G \gg Z$ the order with increasing binding energy is $^9D_6 \ldots {}^9D_2$ and $^7D_1 \ldots {}^7D_5$. The I^{01} spectrum, which measures the correlation $\langle s \cdot S \rangle$, has positive (negative) signal when s and S are parallel (antiparallel). The I^{10} spectrum (to the εd continuum) measures the correlation $\langle \ell \cdot S \rangle$ so that the intensity is positive (negative) for ℓ and S parallel (antiparallel). The nonet and septet states have opposite structures because the order of the J levels is reversed. The spin–orbit spectrum shows negative and positive lobes for each spin state.

The calculation for the transition $LSJ \rightarrow \underline{LSJ}$ can be performed by hand using Wigner–Racah algebra [42] and the result is shown in Fig. 4(a).

9.1.5. Intermediate coupling

The result of the calculation in intermediate coupling using Cowan's code [42] is displayed in Fig. 4(b) and a good agreement is obtained with experimental results [69,72]. Peak A is the nonet state which has clearly distinguishable J levels. Peak B at 6.7 eV and peak D at 30 eV above the leading peak are the only septet states that are clearly visible. The other three septet states have very weak intensities. The intensity of peak C in the measurements is primarily due to inelastic losses. It is interesting to compare Fig. 4(a) and (b). The I^{00} spectrum in intermediate coupling shows that the line intensities in peak A are fairly proportional to $2J + 1$. Also in the I^{10} spectrum, LSJ coupling predicts the line intensities in the ^9D quite well. Thus for this state with stretched spin, LSJ coupling is a good approximation, however, it fails completely to explain the structure in the ^7D states. The electrostatic interaction between the different septet states destroys the regularity of the J level pattern. Experimental corroboration for the magnetic circular dichroism and the spin polarization can be found in Refs. [69,54] and [72], respectively.

9.2. Yb 4f photoemission

In this example we give the fundamental spectra for the rare earth 4*f* photoemission calculated in intermediate coupling. Fig. 5 shows the calculated 4*f* photoemission for the transition Yb $4f^{13} \rightarrow 4f^{12}\varepsilon d$. The Hund's rule ground state $f^{13}\ {}^2F_{7/2}$ ($M_J = -7/2$) is a single Slater determinant with $n_m = 2$ for $-3 \le m \le 2$ and $n_3 = 1$. Substitution of n_m into Eq. (42) gives the integrated intensities $\rho^0 = 13$ and $\rho^{x \neq 0} = -1$, which are linearly proportional to the expectation values of the 4*f* ground state properties, via the sum rules [22,73].

9.3. Diffraction effects

In a solid the emitted photoelectrons will be scattered by the nearby atoms. For crystalline materials the measured core level photoemission is enhanced or suppressed for emission directions along certain crystallographic directions due to photoelectron diffraction.

Fig. 6 shows the magnetic linear dichroism in the angular dependence of the Fe 3*p* photoemission at 170 eV photon energy for normal incidence light and −45° emission angle (see inset of Fig. 6(a)) [74]. The dichroism manifests itself as a change in the Fe 3*p* line shape when the magnetization is reversed. Fig. 6(b) shows the difference spectrum, which is compared to the calculated result

from Ref. [25], with spin–orbit splitting parameter of ζ_{3p} = 0.95 eV and core-level exchange field H_S = 1.3 eV. To account for the finite lifetime and resolution, the theoretical spectra were convoluted with Lorentzians of 0.25 eV for spin-up and 0.9 eV for spin-down states, together with a Gaussian of 0.3 eV. The spectral shape of the dichroism is in good agreement with the experimental result when the spin and orbit dependence of the lifetime broadening is taken into account [25]. Fig. 6 shows the measured angular distribution of the photoemission intensity for the two sample magnetization directions at 51.8 eV binding energy, where the dichroism is maximum (see Fig. 6). The two emission patterns obtained by reversing the magnetization are mirror images of each other. The patterns show four distinct features at ±45° and ±20° emission angles, whose shapes and intensities are affected by reversing the magnetization.

The angular distribution of the MLDAD i.e., the difference between the two angular patterns is also shown in Fig. 6. The linear dichroism has a similar angular dependence, but opposite sign for emission into the adjacent quadrants. Thus, the dichroism in the photoemission integrated over the emission plane vanishes. This means that MLDAD only occurs in angle-resolved photoemission. Despite some distortion due to photoelectron diffraction, the characteristic sin 2θ dependence is clearly visible.

9.4. HAXPES

Recently, hard X-ray PES (HAXPES) emerged as an important extension to soft X-ray and ultraviolet photoemission. It offers a more bulk sensitively probe due to a much longer electron mean free path (typically 2-10 nm). This means that HAXPES enables the nondestructive analysis of buried layers and interfaces, and the discrimination of bulk and surface related features.

Photoemission studies of $Ga_{1-x}Mn_xAs$ have indicated the importance of Mn diffusion and surface buildup during low-temperature annealing. HAXPES 'bulk' measurements of the MCD and MLDAD in the Mn 2p photoemission are shown in Fig. 7, which shows that both type of measurements give the same fundamental spectrum I^1 with its typical $(-++-)$ signature [75,76]. The geometry for MLDAD is shown in Fig. 8(c), where the emission distribution is independent of the sample surface orientation.

The interference term, which determines the magnitude and sign of the MLDAD, depends strongly on the kinetic energy [25,27]. Fig. 8(a) shows the kinetic energy dependence of the radial matrix elements R_s and R_d for emission from the Mn 2p to the s and d continua together with the phase difference δ between the outgoing waves. Using Eqs. (61) and (62), we obtain the kinetic energy dependence of the normalized MCD and MLDAD signals, respectively, shown in Fig. 8(b) for the ideal measurement geometry. Since $R_d^2 \gg R_s^2$, the XMCD intensity is essentially flat with a small energy dependence due to the interference term. It is useful to mention that the situation is rather different for 3p emission, where $R_d^2 \ll R_s^2$ below ~30 eV, so that the sign of the MCD reverses [25,27].

The MLDAD, which depends entirely on the interference term, vanishes for sin δ = 0 (at ~530 eV) and reaches optimal values near sin δ = ±1 (at ~50 and ~5450 eV). Therefore, a high photon energy of several keV is very beneficial for MLDAD measurement, while at the same time it permits to capture the bulk magnetic properties due to the large electron mean free path. Moreover, high kinetic energies ensure that the outgoing electron has negligible interaction with the atom left behind, which is an important criterium for accurate model calculations. The price to pay is of course the strongly diminished cross section at high energies.

Simulations of the spectra using an Anderson impurity model show that the ferromagnetic Mn 3d electrons of substitutional Mn in (Ga,Mn)As are intermediate between localized and delocalized [76,75,77].

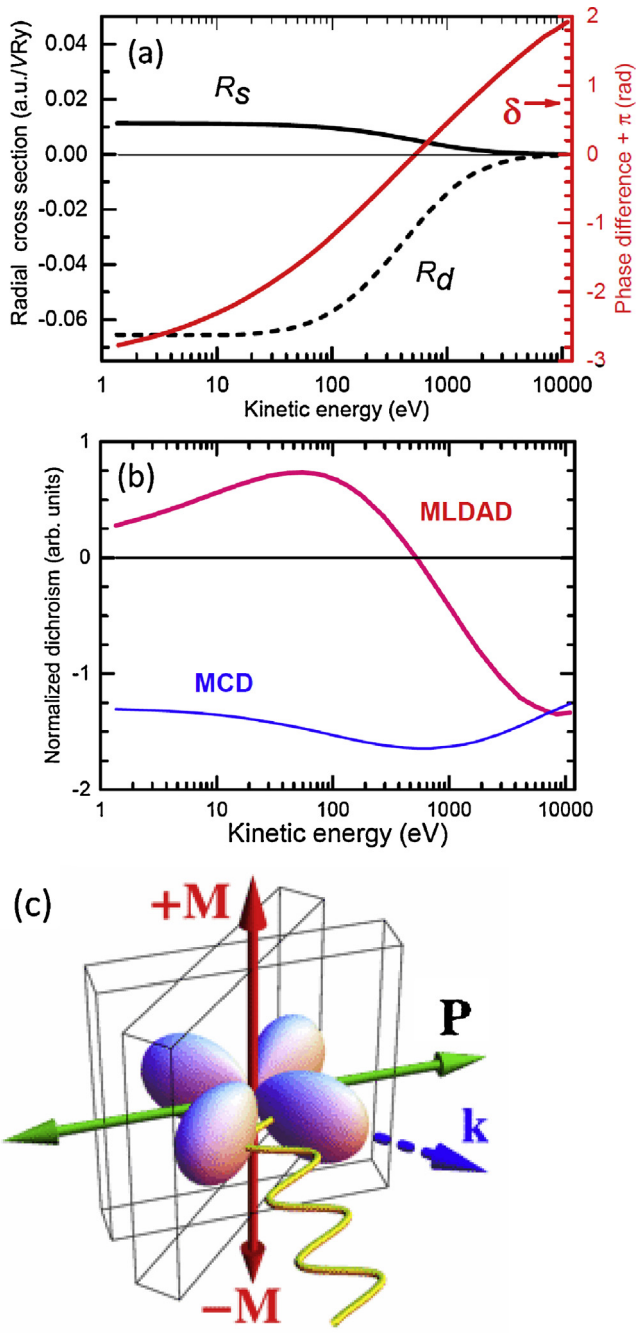

Fig. 8. Kinetic energy dependence of Mn 2p photoemission. (a) The radial matrix elements R_s (black line) and R_d (black dashed line) for emission from the Mn 2p to the s and d continua with the phase difference δ (red line). (b) The MCD and MLDAD signals calculated using Eq. (61) and (62), respectively, for the ideal geometry (for MCD: $\mathbf{M} \parallel \mathbf{P} \parallel \varepsilon$). Both dichroic signals have been normalized by division by the total intensity ($R_s^2 + 2R_d^2$). (c) The chiral geometry for **M**, **P**, and ε, used in the MLDAD experiment showing possible sample positions. The angular distribution $\varepsilon(\theta, \phi)$ is proportional to $\sin^2\theta \sin 2\phi$, where $\pm\mathbf{M} \| z$, $\mathbf{P} \| x$. For the ideal geometry, ε is along **k**.

10. Conclusions

The different ways to orient the polarizations of the magnetization, electric vector of the light, and the spin of the photoelectron allow us to measure the different kinds of correlations between corresponding atomic properties: the valence spin, core hole orbital moment and core hole spin, respectively. We can define fundamental spectra as those linear combinations of the polarized spectra that are directly connected to physical properties. Magnetic dichroism

in core level photoemission, which gives the alignment between the valence spin magnetic moment and the core hole orbital moment, requires both spin–orbit and electrostatic interactions. For the emission from an incompletely filled localized shell, such as the $4f$ in the rare earths, the integrated intensities of the magnetic circular dichroism and the spin spectrum are proportional to the ground state orbital and spin magnetic moment, respectively. In angle integrated photoemission the light polarizaton and the induced moment of the atom have the same parity, so that the linearly polarized light measure only even moments, and circular polarization measures only odd (magnetic) moments. However, when the light polarization vector, the z-axis of the system (e.g., the molecular axis or the magnetic axis) and the emission direction of the photoelectron are not coplanar, the experimental geometry is not a mirror image of itself. Then the interference term between the ℓ+1 and $\ell-1$ channels no longer cancels but depends on the radial matrix element and the phase difference of these channels and we can measure even moments with odd polarized light and odd moments with even polarized light. Thus the photoemission spectrum measured in magnetic circular dichroism can also be obtained using linear polarized radiation in a chiral geometry.

The core-hole polarization can be used as a probe of the ground-state properties. X-ray absorption measures only the monopole term of the core hole, but when the core hole is decaying under emission of electrons or photons, the angular dependence gives information about the anisotropy of the core hole. The intensity is a sum over ground-state moments times the probability to create a polarized core hole using polarized light, times the probability for decay of such a core hole into the final state. The core polarization analysis generalises the use of sum rules in X-ray absorption spectroscopy, where the integrated peak intensities give ground state expectation values of operators such as the spin and orbital moments. The photoemission decay makes it possible to measure different linear combinations of the tensor operators.

References

[1] H. Hertz, Ann. Phys. 31 (1887) 983.
[2] A. Einstein, Ann. Phys. 17 (1905) 132.
[3] L. Baumgarten, C.M. Schneider, H. Petersen, F. Schäfers, J. Kirschner, Phys. Rev. Lett. 65 (1990) 492.
[4] G.D. Waddill, J.G. Tobin, D.P. Pappas, Phys. Rev. B 46 (1992) 552.
[5] D. Venus, L. Baumgarten, C.M. Schneider, C. Boeglin, J. Kirschner, J. Phys.: Condens. Matter 5 (1993) 1239.
[6] C.M. Schneider, D. Venus, J. Kirschner, Phys. Rev. B 45 (1992) 5041.
[7] G. van der Laan, M.A. Hoyland, M. Surman, C.F.J. Fipse, B.T. Thole, Phys. Rev. Lett. 69 (1992) 3827.
[8] L.H. Tjeng, C.T. Chen, P. Rudolf, G. Meigs, G. van der Laan, B.T. Thole, Phys. Rev. B (1993) 13378.
[9] C. Roth, H.B. Rose, F.U. Hillebrecht, E. Kisker, Solid State Commun. 86 (1993) 647.
[10] C. Roth, F.U. Hillebrecht, H.B. Rose, E. Kisker, Phys. Rev. Lett. 70 (1993) 3479.
[11] F. Sirotti, G. Rossi, Phys. Rev. B 22 (1994) 15682.
[12] B. Thole, G. van der Laan, Phys. Rev. B 49 (1994) 9613.
[13] G. van der Laan, B.T. Thole, Solid State Commun. 92 (1994) 427.
[14] G.H. Fecher, V.V. Kuznetsov, N.A. Cherepkov, G. Schönhense, J. Electron Spectrosc. Rel. Phenom. (2002) 157.
[15] G. van der Laan, M. Taguchi, Phys. Rev. B 82 (2010) 045114.
[16] T. Gouder, G. van der Laan, A.B. Shick, R.G. Haire, R. Caciuffo, Phys. Rev. B 83 (2011) 125111.
[17] C.E. ViolBarbosa, S. Ourdi, G.H. Fecher, D. Ebke, C. Felser, J. Electron Spectrosc. Rel. Phenom. 189 (2013) 146.
[18] U. Heinzmann, J.H. Dil, J. Phys.: Condens. Matter (2012) 173001.
[19] G. van der Laan, C. Westra, C. Haas, G.A. Sawatzky, Phys. Rev. B 23 (1981) 4369.
[20] I. Talmi, Simple Models of Complex Nuclei – The Shell Model and Interacting Bosom Model, Harwood Academic Publishers, Chur, Switzerland, 1993.
[21] B.T. Thole, G. van der Laan, Phys. Rev. B 44 (1991) 12424.
[22] G. van der Laan, B.T. Thole, Phys. Rev. B 48 (1993) 210.
[23] G. van der Laan, B.T. Thole, Phys. Rev. B 52 (1995) 15355.
[24] G. van der Laan, Phys. Rev. Lett. 66 (1991) 2527.
[25] G. van der Laan, Phys. Rev. B 51 (1995) 240.
[26] B.T. Thole, G. van der Laan, Phys. Rev. B 50 (1994) 11474.
[27] G. van der Laan, Phys. Rev. B 55 (1997) 3656.
[28] A. Messiah, Quantum Mechanics, Dover Publications, Mineola, NY, 1999.
[29] G. van der Laan, A.I. Figueroa, Coord. Chem. Rev. 277–278 (2014) 95.
[30] M. van Veenendaal, Theory of Inelastic Scattering and Absorption of X-rays, Cambridge University Press, Cambridge, UK, 2015.
[31] G. van der Laan, B.T. Thole, J. Phys.: Condens. Matter 7 (1995) 9947, App. B.
[32] A.P. Yutsis, I.B. Levinson, V.V. Vanagas, Mathematical Apparatus of the Theory of Angular Momentum, Israel Program for Scientific Translation, Jerusalem, 1962.
[33] D.M. Brink, G.R. Satchler, Angular Momentum, Oxford University Press, London, 1962.
[34] D.A. Varshalovich, A.N. Moskalev, V.K. Khersonskii, Quantum Theory of Angular Momentum, World Scientific, Singapore, 1988, pp. 302.
[35] H. Ebert, J. Phys.: Condens. Matter 1 (1989) 9111.
[36] G. van der Laan, in: P. Bagus, F. Parmigiani, G. Pacchioni (Eds.), Core Level Spectroscopies for Magnetic Phenomena: Theory and Experiment, Plenum, New York, 1995, pp. 153–171.
[37] G. van der Laan, J. Electron Spectrosc. Relat. Phenomen. 117-118 (2001) 89.
[38] G. van der Laan, Phys. Rev. Lett. 82 (1999) 640.
[39] H.A. Dürr, G. van der Laan, D. Spanke, F.U. Hillebrecht, N.B. Brookes, Europhys. Lett. 40 (1997) 171.
[40] G. Panaccione, G. van der Laan, H.A. Dürr, J. Vogel, N.B. Brookes, Eur. Phys. J. B 19 (2001) 281.
[41] G. Panaccione, H.A. Dürr, J. Vogel, N.B. Brookes, G. van der Laan, J. Magn. Magn. Mater. 233 (2001) 57.
[42] R.D. Cowan, The Theory of Atomic Structure and Spectra, University of California Press, Berkeley, 1981.
[43] G. van der Laan, B.T. Thole, J. Phys.: Condens. Matter 7 (1995), 9947, App. A.
[44] B.T. Thole, P. Carra, F. Sette, G. van der Laan, Phys. Rev. Lett. 68 (1992) 1943.
[45] P. Carra, B.T. Thole, M. Altarelli, X. Wang, Phys. Rev. Lett. (1993) 694.
[46] P. Carra, H. König, B.T. Thole, M. Altarelli, Physica B 192 (1993) 182.
[47] G. van der Laan, B.T. Thole, Phys. Rev. B 53 (1996) 14458.
[48] G. van der Laan, Phys. Rev. B 57 (1998) 112.
[49] P. Dalmas de Réotier, A. Yaouanc, G. van der Laan, N. Kernavanois, J.-P. Sanchez, J.L. Smith, A. Hiess, A. Huxley, A. Rogalev, Phys. Rev. B 60 (1999) 10606.
[50] B.R. Judd, Second Quantization and Atomic Spectroscopy, Johns Hopkins Press, Baltmore, 1967.
[51] B.T. Thole, G. van der Laan, M. Fabrizio, Phys. Rev. B 50 (1994) 11466.
[52] Y. Liu, Z. Xu, P.D. Johnson, G. van der Laan, Phys. Rev. B 52 (1995) R8593.
[53] G. Panaccione, P. Torelli, G. Rossi, G. van der Laan, M. Sacchi, F. Sirotti, Phys. Rev. B 58 (1998) R5916.
[54] G. Panaccione, P. Torelli, G. Rossi, G. van der Laan, P. Prieto, F. Sirotti, J. Phys.: Condens. Matter 11 (1999) 3431.
[55] C. Roth, F.U. Hillebrecht, W.G. Park, E. Kisker, Phys. Rev. Lett 73 (1994) 1963.
[56] J.S. Lomont, Applications of Finite Groups, Academic Press, New York, 1959.
[57] P.H. Butler, Point Group Symmetry, Applications, Methods and Tables, Plenum, New York, 1981.
[58] G. van der Laan, J. Phys. Soc. Jpn 63 (1994) 2393.
[59] G. van der Laan, Phys. Rev. B 55 (1997) 8086.
[60] G. van der Laan, J. Phys.: Condens. Matter 9 (1997) L259.
[61] G. van der Laan, Appl. Phys. A 65 (1997) 135.
[62] B.T. Thole, H.A. Dürr, G. van der Laan, Phys. Rev. Lett. 74 (1995) 2371.
[63] H.A. Dürr, G. van der Laan, M. Surman, J. Phys.: Condens. Matter 8 (1996) L7.
[64] G. van der Laan, J. Electron Spectrosc. Relat. Phenomen. 101–103 (1999) 859.
[65] G. van der Laan, Appl. Phys. A 73 (2001) 673.
[66] G. van der Laan, H.A. Dürr, M. Surman, J. Electron Spectrosc. Relat. Phenomen. 78 (1996) 213.
[67] L. Braicovich, A. Tagliaferri, G. van der Laan, G. Ghiringhelli, N.B. Brookes, Phys. Rev. Lett. 90 (2003) 117401.
[68] G. van der Laan, G. Ghiringhelli, A. Tagliaferri, N.B. Brookes, L. Braicovich, Phys. Rev. B 69 (2004) 104427.
[69] G. van der Laan, E. Arenholz, E. Navas, A. Bauer, G. Kaindl, Phys. Rev. B 53 (1996) R5998.
[70] G. van der Laan, E. Arenholz, E. Navas, Z. Hu, E. Mentz, A. Bauer, G. Kaindl, Phys. Rev. B 56 (1997) 3244.
[71] E. Arenholz, E. Navas, K. Starke, L. Baumgarten, G. Kaindl, Phys. Rev. B (1995) 8211.
[72] W.J. Lademan, A.K. See, L.E. Klebanoff, G. van der Laan, Phys. Rev. B 54 (1996) 17191.
[73] B.T. Thole, G. van der Laan, Phys. Rev. Lett 70 (1993) 2499.
[74] F.U. Hillebrecht, H.B. Rose, T. Kinoshita, G. van der Laan, R. Denecke, L. Ley, Phys. Rev. Lett 75 (1995) 2883.
[75] J. Fujii, B.R. Salles, M. Sperl, S. Ueda, M. Kobata, Y. Yamashita, P. Torelli, M. Utz, C.S. Fadley, A.X. Gray, J. Braun, H. Ebert, I. Di Marco, O. Eriksson, P. Thurnström, G.H. Fecher, H. Stryhanyuk, E. Ikenaga, J. Minár, C.H. Back, G. van der Laan, G. Panaccione, Phys. Rev. Lett 111 (2013) 097201.
[76] K.W. Edmonds, G. van der Laan, N.R.S. Farley, R.P. Campion, B.L. Gallagher, C.T. Foxon, B.C.C. Cowie, S. Warren, T.K. Johal, Phys. Rev. Lett. 107 (2011) 197601.
[77] K.W. Edmonds, G. van der Laan, G. Panaccione, Semicond. Sci. Technol. 30 (2015) 043001.